学位論文

Design Study on Fast-Ignition Laser Fusion Reactor with a Dry Wall Chamber

（固体壁チェンバーを用いた高速点火方式レーザー核融合炉設計研究）

2007 年度

提出先

東京大学大学院新領域創成科学研究科
基盤科学系先端エネルギー工学専攻

後藤　拓也

Abstract

The design study of fast-ignition laser fusion reactor with a dry wall chamber has been carried out. Fusion energy is expected to be a possible candidate for an alternative energy source in near future. Laser fusion is one of the possible method to achieve fusion burn, which produces extremely dense plasma by an irradiation of intense laser beams to a tiny fuel pellet with a high spherical symmetry. The fast ignition scheme, a new challenging path to achieve ignition and burn of the compressed pellet by the external heating with an ultra-intense laser, can reduce the target yield per a shot to the one order compared with the conventional central ignition scheme with keeping the sufficient gain for a commercial reactor. This small target yield may enable the design of a compact dry wall chamber, which is free from several difficulties and restrictions in the development and the use of a liquid wall chamber. It also enables a simple cask maintenance method for the replacement of the blanket system. In this paper the conceptual design of the laser fusion reactor, which makes full use of the fast ignition scheme with a consideration of the physics and engineering issues as a commercial fusion power plant, was discussed.

This paper emphasized on the core plasma design and the feasibility study of a dry wall chamber. In the core plasma design, the optimization of the pellet design and the laser pulse shaping from the viewpoint of the minimization of the target yield and the utilization of the fast ignition scheme was discussed through the numerical analysis by using 1-D and 2-D hydrodynamic simulation code. In the feasibility study of a dry wall chamber, thermomechanical analysis and consideration of multiple aspects about the threatening effects due to the pulse heat and particle load were carried out. These analyses revealed the possibility of the plant design with one pulse target yield of 40 MJ and the dry wall chamber with 5–6 m radius. Then the commercial power plant with 400 MWe electric power was proposed with 30 Hz repetition of laser irradiation by considering the possible chamber evacuation and pellet injection method. According to the economic analysis by using the developed system analysis code, the total capital cost of this plant is estimated to be about 400 billion yen, 1.5 to 2 times higher than a present nuclear fission plant. This relatively low construction cost and the high engineering reliability and feasibility accompanied with the use of a dry wall give a great impact on the development of not only laser fusion but also whole fusion energy science. Whereas this design requires the efficient heating of the compressed fuel pellet without a cone guide and the development of the material for the first wall armor that has high resistance to cyclic heat load and surface morphological change due to

high energy particle irradiation Therefore, further research, especially in experimental study, is required to clarify the possibility of this laser fusion reactor design with a compact dry wall chamber.

Contents

List of Figures

List of Tables

Chapter 1

Introduction

1.1 Nuclear fusion and fusion energy source

Nuclear fusion is one of the nuclear reaction in which two light nuclei are combined and produce a heavier nucleus. The sum of the mass of produced particles is slightly smaller than that of initial particles and this mass deficiency is released as an kinetic energy of the produced particles.

Nuclear fusion is considered to be the energy source of fixed stars like the sun. In fixed stars, four protons are converted to one helium through three reactions as described below:

$$\mathrm{p} + \mathrm{p} \rightarrow \mathrm{d} + \beta^{+} + \nu + 1.2 \text{ MeV} \tag{1.1}$$

$$\mathrm{p} + \mathrm{d} \rightarrow \mathrm{h} + 5.5 \text{ MeV} \tag{1.2}$$

$$\mathrm{h} + \mathrm{h} \rightarrow \alpha + 2\mathrm{p} + 12.9 \text{ MeV} \tag{1.3}$$

where p, d, h represent proton, deuteron and helium-3 nucleus, respectively. However, the above reactions have a very slow reaction rate and occur only under the special condition in the core of fixed stars (extremely high density (1.56×10^5 kg/m^3) and relatively low temperature ($\sim 10^7$ K)). The fusion reaction expected to be used the first for power generation is the D-T reaction:

$$\mathrm{d} + \mathrm{t} \rightarrow n + \alpha + 17.6 \text{ MeV} . \tag{1.4}$$

Other accessible fusion reactions are following three ones:

$$\mathrm{d} + \mathrm{d} \rightarrow \begin{cases} \mathrm{p} + \mathrm{t} + 4.1 \text{ MeV} \\ n + \mathrm{h} + 3.2 \text{ MeV} \end{cases} \quad (\text{D-}^3\text{He reaction}) \tag{1.5}$$

$$\mathrm{d} + \mathrm{h} \rightarrow \mathrm{p} + \alpha + 18.3 \text{ MeV} \quad (\text{D-}^3\text{He reaction}) \tag{1.6}$$

$$\mathrm{p} + {}^{11}\mathrm{B} \rightarrow 3\alpha + 8.7 \text{ MeV} \quad (\text{p-B reaction}) \tag{1.7}$$

From the viewpoint as an energy source, nuclear fusion has similar characteristics to nuclear fission, that is already in a commercial use as a nuclear fission plant. For example, nuclear fusion has a large

energy density. It also produces no carbon dioxide that is considered to be the main cause of the global climate change. In addition, fusion reaction itself produces no radioactive material except for tritium from D-D reaction. In D-T reaction, tritium itself is a radioactive material. But it is produced through the neutron reaction of lithium in the plant and there is no need of the transportation of radioactive fuel. In D-T and D-D reactions, however, produced fast neutrons irradiate and activate the components surrounding the reactor chamber. Since D-^{3}He reaction is inevitably accompanied with D-D reaction, it also produce slight amount of neutron and tritium. Thus, fusion reactions except for p-B reaction are not free from nuclear wastes. However, produced radioactive materials do not contain high level waste (HLW) and they become under the clearance level within about 100 years. Therefore nuclear fusion is considered to be one option of the future energy source, especially for large-scale and centralized electric power generation.

The number of D-T fusion reaction per unit time, per unit volume N_{DT} is described as

$$N_{\mathrm{DT}} = n_{\mathrm{D}} n_{\mathrm{T}} \langle \sigma v \rangle_{\mathrm{DT}} \tag{1.8}$$

where n_{D}, n_{T} are densities of deuteron and triton, respectively. $\langle \sigma v \rangle_{\mathrm{DT}}$ is the D-T fusion reaction cross-section averaged by the Maxwellian velocity distribution. Apparently, high densities of react nuclei and high reaction cross-section are required to achieve sufficient fusion reaction. Figure 1.1 shows the reaction cross-sections of D-T, D-D and D-^{3}He reaction as the function of ion temperature.

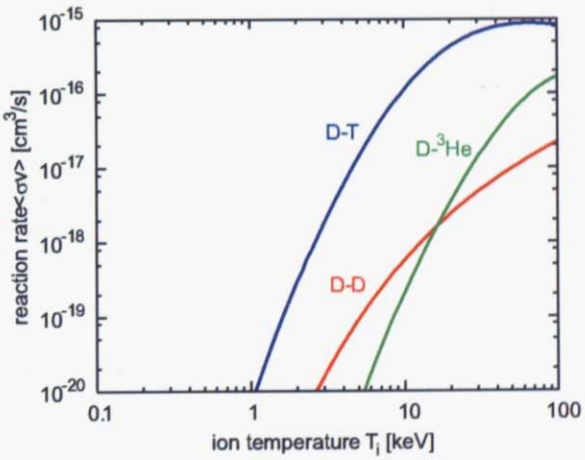

Fig. 1.1: Reaction cross-sections of D-T, D-D and D-^{3}He reaction

Therefore, it is required to keep high density, high temperature state for the time within which the sufficient fusion reaction occurs. There are two main methods to achieve such condition. One is the magnetic fusion, which uses a strong magnetic field (several Tesla) produced by superconducting

conductors to confine a high temperature ($\sim$ 10 keV) plasma with density of $\sim 10^{20}$ m^{-3} for relatively long time ($\sim$ 1 sec). The other is the inertial fusion. The inertial fusion uses an intense laser or an ion beam to produce an extremely high density ($\sim 10^{31}$ m^{-3}) plasma for a very short time ($\sim 10^{-12}$ sec). The detailed description of the principle of the inertial fusion is given in Chapter 2.

1.2 Motivation of this research

As mentioned in the previous section, fusion energy is considered to be a probable option of the future energy source. Thus research in controlled fusion is quite meaningful to propose a solution for the energy problem.

The research in fusion is now at the phase in which a great breakthrough, the demonstration of fusion burn, is achieved. Although many physics and engineering research and development (R&D) issues need to be solved before realizing a commercial fusion power plant, a conceptual design of a commercial plant is quite important to clarify the physics and engineering issues.

In the magnetic confinement fusion, several proposals of such conceptual design have been given by many researchers in the world [1–5]. Whereas the inertial fusion has quite different properties and it is quite important to progress the research with considering the difference and commonality between the magnetic fusion and the inertial fusion.

In the inertial fusion, some design studies have already been carried out as shown in table 1.1. The most critical problem in the design of an inertial fusion reactor is its high heat and particle load on the chamber first wall. Then KOYO and KOYO-Fast reactor, designed by Osaka University [6, 7], adopt a liquid metal wall, the protection of chamber wall by a thin liquid metal layer, to accommodate a high heat load. However, liquid wall has several engineering issues: how to produce a uniform thin liquid metal layer on the metallic structural components, how to cover the chamber ceiling or the edge of beam ports. In addition, in such liquid wall system, evaporated liquid metal interferes the succeeding pellet injection and laser irradiation, that leads to the decrease of the laser usability. Then in the designs of KOYO and KOYO-Fast reactor, a novel idea of the multi-chamber concept, four chambers alternatively irradiated by a single laser system, was proposed But it may require a complicated laser transmission system. Whereas in the US HAPL project [8], the use of a dry wall chamber has been considered. However it adopts conventional central ignition scheme, and then the chamber radius tends to be larger ($\sim$ 10 m). Since the heat load on the first wall is still very high with such a large size chamber, the idea of magnetic intervention, using cusp coils to guide ions to the specific heat sink components, has been also proposed [9].

Table 1.1: Comparison of main parameters of past IFE reactor designs with FALCON-D (the reactor designed in this study).

	KOYO	KOYO-Fast	HAPL	FALCON-D
chamber radius [m]	4	3	11	5~6
ignition method	central ignition	fast ignition	central ignition	fast ignition
chamber wall	liquid wall		dry wall*1	dry wall
injection energy $E_{\rm in}$[MJ] (implosion / heating)	3.4	1.2 (1.13/0.07)	2.36*2	0.4 (0.35/0.05)
pellet gain G	176	167	148	100
target yield $E_{\rm fus}$[MJ]	600	200	350	40
wall load (except neutron) [J/cm2]	60	35	4.6	~ 2.0
repetition rate $f_{\rm rep}$[Hz]	$12(3 \times 4)$	$16(4 \times 4)$	5	30
fusion output $P_{\rm fus}$[MW]	7200	3200	1750	1200

*1 Also considering the magnetic intervention method [9] .
*2 Not found in the reference; calculated from the fusion gain and target yield.

However, fast ignition scheme can reduce the target yield (fusion output per one shot) ten times smaller than conventional central ignition scheme. Thus it may enable the design of a compact dry wall chamber, which has high engineering reliability. In addition, fast ignition can alleviate several physics requirements for pellet implosion. It leads to much flexibility in the pellet design and the laser pulse shaping. These characteristics also can reduce the number of laser beams, that leads to a simple maintenance method. Therefore it is meaningful to examine the feasibility of such design as an alternative option for a commercial laser fusion power plant.

Then we started to study about the laser fusion reactor design that makes full use of the fast ignition scheme with consideration of physics and engineering issues for a commercial plant. The research described in this paper consists a part of the design study of fast ignition laser fusion reactor with a dry wall chamber, FALCON-D (Fast ignition Advanced Laser fusion reactor CONcept with a Dry wall chamber), carried out by the collaboration work of the University of Tokyo, Central Research Institute of Electric Power Industry (CRIEPI), and Musashi Institute of Technology.

In chapter 2 the basic physics of IFE is briefly reviewed. Chapter 3 describes the design concept of FALCON-D. Chapter 4 gives the core plasma design through numerical simulation by one-dimensional hydrodynamic code ILESTA-1D. Chapter 5 describes the feasibility analysis of the design of a dry wall chamber. Chapter 6 describes the overall plant system design and reference plant parameters. Chapter 7 gives some discussion and clarifies the required research and development issues through the comparison of other IFE reactor designs and magnetic fusion reactor designs.

Chapter 2

Review of the Laser Fusion Concept

In inertial fusion, the process called "implosion" is indispensable. The process of implosion is schematically shown in Fig. 2.1. First, a D-T fuel pellet with the shape of a spherical shell is directly or indirectly irradiated by a laser or a ion beam with high spherical symmetry. The material which surrounds the main fuel (called as an "ablator") absorbs this energy and ablates. Then the internal fuel is accelerated to the center by the counter action and compressed to high density. In the next section, basic physics of the inertial fusion is briefly reviewed. Then one can find the reason why implosion is necessary the for the inertial fusion. In the succeeding sections, the two schemes to achieve implosion and fusion burn of the fuel, central ignition and fast ignition, are reviewed. The related issues about a hydrodynamic instability are also discussed.

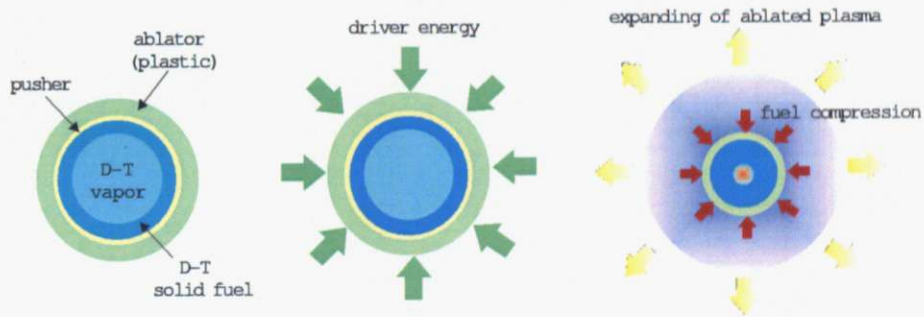

Fig. 2.1: Schematic view of an implosion process

2.1 Basic concept of the inertial fusion

2.1.1 Power flow and fusion gain of an IFE reactor

Figure 2.2 shows the power flow in an IFE reactor. As you can see, the gross electric output P_e is the product of driver power P_d, driver efficiency η_d, fusion gain G (fusion output energy divided by the

injected energy), energy multiplication by neutron reaction in the blanket M, and thermal efficiency $\eta_{\rm th}$;

$$P_{\rm e} = \eta_{\rm d} G M \eta_{\rm th} P_{\rm d}, \qquad \frac{P_{\rm g}}{P_{\rm d}} = \eta_{\rm d} G M \eta_{\rm th} \ . \tag{2.1}$$

The net electric output $P_{\rm e,net}$ is obtained by subtracting driver power $P_{\rm d}$ and other recirculation power

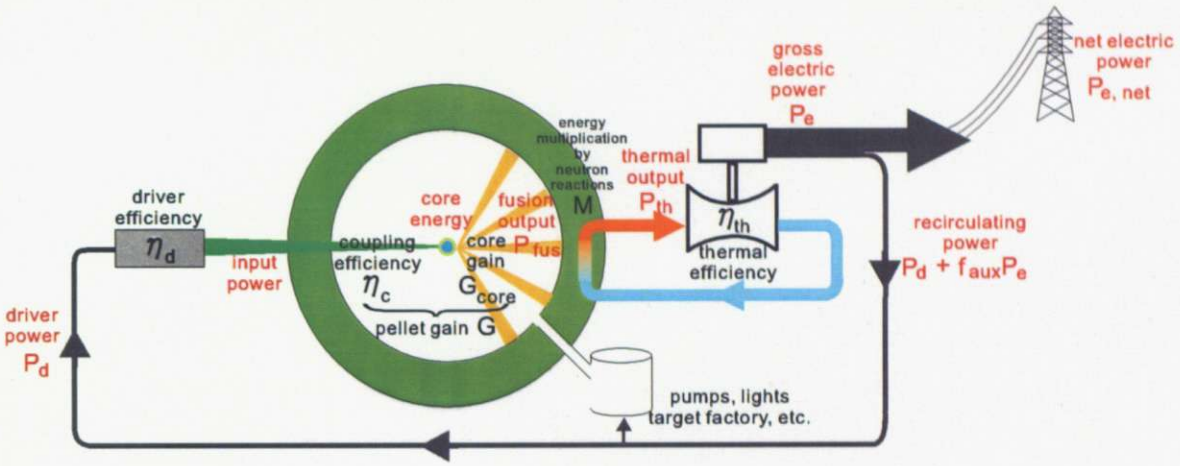

Fig. 2.2: Power flow in an IFE reactor

$P_{\rm aux}$ from the gross electric output. Assuming the recirculation power accounts for the constant fraction ($f_{\rm aux}$) of gross electric power, the net electric output is given as

$$P_{\rm e,net} = P_{\rm e} - P_{\rm aux} - P_{\rm d} = P_{\rm e}\left(1 - f_{\rm aux} - \frac{1}{\eta_{\rm d} G M \eta_{\rm th}}\right) \ . \tag{2.2}$$

The relation between the parameter $\eta_{\rm d} G$ and the fraction of net electric output to the gross one (in case of $f_{\rm aux} = 5\%$) is shown in Fig. 2.3. For a commercial operation, the recirculation power should be suppressed below 25 % of the gross electric output. Figure 2.3 indicates that $\eta_{\rm d} G \gtrsim 10$ is required. Since in practice the driver efficiency $\eta_{\rm d}$ is in the range of 5–15 %, the fusion gain of $G = 90$–200 is required. The achievement of such high fusion gain is the most important factor in the inertial fusion. Here fusion gain is defined as the ratio of energy released from the fuel pellet through fusion reaction $E_{\rm fus}$ to that injected into the pellet $E_{\rm in}$; $G = E_{\rm fus}/E_{\rm in}$. Fusion energy output is described as the product of D-T reaction energy per unit mass $Q_{\rm DT}$ ($= 3.4 \times 10^{11}$ J/g), the total mass of the pellet $M_{\rm f}$, and burn fraction $f_{\rm b}$;

$$E_{\rm fus} = Q_{\rm DT} M_{\rm f} f_{\rm b} \ . \tag{2.3}$$

the detailed physics mechanism which determines the burn fraction is described in the next subsection.

Core gain is defined as the ratio of fusion energy to the energy content in the fuel core $E_{\rm f}$; $G_{\rm f} =$

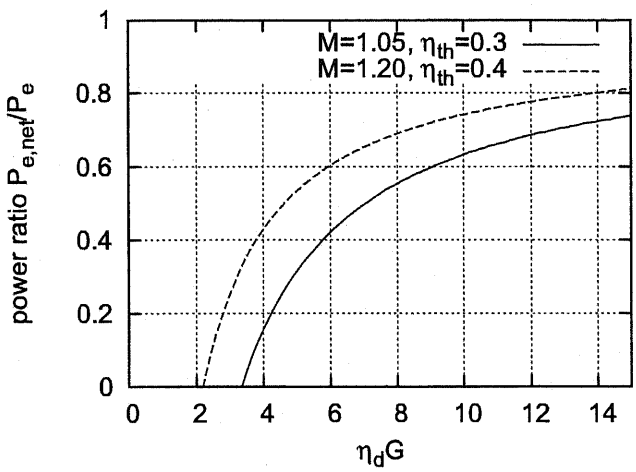

Fig. 2.3: The fraction of net electric output to gross one $P_{\mathrm{e,net}}/P_{\mathrm{e}}$ vs. the product of driver efficiency and pellet gain $\eta_{\mathrm{d}}G$

$E_{\mathrm{fus}}/E_{\mathrm{f}}$. Let conversion efficiency from injection energy to fuel core is η_{c}, core gain is related to fusion gain through the formula $G = \eta_{\mathrm{c}}G_{\mathrm{f}}$.

Consequently, in order to achieve high fusion gain, it is required to:

- increase burn fraction f_{b}
- increase core gain G_{f}
- increase coupling efficiency η_{c}

2.1.2 Burn fraction

Burn fraction is defined as

$$f_b = 1 - \frac{n}{n_0} \tag{2.4}$$

where n_0 and n are the initial density and the density after burning, respectively.

If a fuel is perfectly confined, temporal evolution of the fuel density can be described with the following differential equation;

$$\frac{\mathrm{d}n_{\mathrm{T}}}{\mathrm{d}t} = -n_{\mathrm{T}}n_{\mathrm{D}}\langle\sigma v\rangle \tag{2.5}$$

where $\langle\sigma v\rangle$ is the D-T reaction cross-section averaged over the Maxwell velocity distribution. Assuming equal densities of react ions ($n_{\mathrm{D}} = n_{\mathrm{T}} = n/2$), Eq. (2.5) can be rewritten as

$$\frac{\mathrm{d}(n/2)}{\mathrm{d}t} = -\frac{n^2}{4}\langle\sigma v\rangle \ . \tag{2.6}$$

By solving the above equation, one can obtain the density as the function of time;

$$n(t) = \frac{1}{\langle\sigma v\rangle t/2 + 1/n_0} = \frac{n_0}{n_0\langle\sigma v\rangle t/2 + 1} \tag{2.7}$$

Here n in Eq. (2.4) is the density just after the fusion burn. Assuming the time at the end of burning to be τ_b, this density is $n(\tau_\mathrm{b})$ in Eq. 2.7.

In an IFE, fusion burn ceases due to the decrease of ion temperature (i.e., reaction rate) accompanied with the fuel expansion. The expansion of such an isolated fluid can be described as the propagation of a rarefaction wave from the surface of the fluid. A rarefaction wave propagates with the sound velocity $c_\mathrm{s} \sim \sqrt{10/3}\, v_{i,\mathrm{th}}$. Then if the wave propagates from the surface of a sphere with radius R, the mean burning mass during the time in which the rarefaction wave reaches to the center R/c_s is given as [10]

$$\langle m(t)\rangle = \frac{\displaystyle\int_0^{R/c_\mathrm{s}} \frac{4\pi\rho}{3}(R - c_\mathrm{s}t)^3\, dt}{R/c_\mathrm{s}} = \frac{m_0}{4} \tag{2.8}$$

where $m_0 = m(t = 0)$. Then effective burn time τ_b is given by

$$\tau_\mathrm{b} = \frac{R}{4c_\mathrm{s}} \tag{2.9}$$

because $\langle m(t)\rangle\tau_\mathrm{b} = m_0\, R/c_\mathrm{s}$. Substituting Eq. (2.7) into Eq. (2.4), one can obtain

$$f_\mathrm{b} = 1 - \frac{n(\tau_\mathrm{b})}{n_0} = 1 - \frac{1}{n_0\langle\sigma v\rangle\tau_\mathrm{d}/2 + 1} = \frac{n_0\langle\sigma v\rangle\tau_\mathrm{b}/2}{n_0\langle\sigma v\rangle\tau_\mathrm{b}/2 + 1} \tag{2.10}$$

where $n_0 = \rho_\mathrm{f}/m_i$, and ρ_f and m_i are the initial fuel density and ion mass, respectively. Substituting Eq. (2.9) into Eq. (2.10), burn fraction is finally described as

$$f_\mathrm{b} = \frac{\rho_\mathrm{f}R_\mathrm{f}}{\rho_\mathrm{f}R_\mathrm{f} + \beta(T)} \tag{2.11}$$

where R_f is fuel radius and $\beta(T) = \dfrac{8m_i c_\mathrm{s}}{\langle\sigma v\rangle}$. Figure 2.4 shows the burn fraction for typical ion temperatures as the function of $\rho_\mathrm{f}R_\mathrm{f}$ value. As described in the following, $f_\mathrm{b} \geq 30$ % is needed to achieve the sufficient fusion gain. Then $\rho_\mathrm{f}R_\mathrm{f} = 10$ g/cm^2 is required for $T_i = 10$keV, 3 for 40 keV.

Consequently, inertial fusion requires not only high temperature to achieve the sufficient fusion reaction cross-section but also high $\rho_\mathrm{f}R_\mathrm{f}$ value to obtain the sufficient pellet gain.

2.1.3 Fuel compression

In order to achieve high $\rho_\mathrm{f}R_\mathrm{f}$ value, it is required to increase the size or density of the fuel pellet. Since fuel mass is proportional to $\rho_\mathrm{f}R_\mathrm{f}^3$, increase of the density, i.e., compression of the fuel, is favorable to reduce the required injection energy.

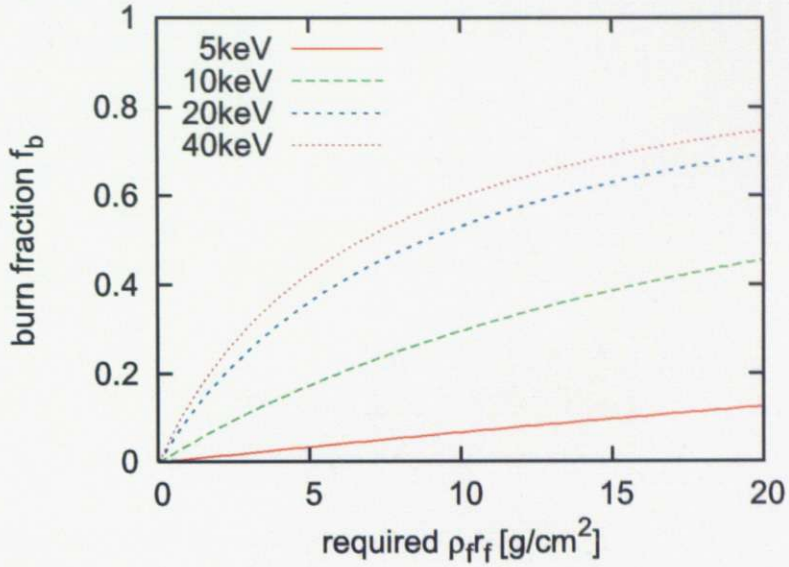

Fig. 2.4: Dependence of burn fraction on the areal density of the compressed fuel$\rho_f R_f$

For example, to achieve $\rho_f R_f > 10$ g/cm^2 by fuel compression, fuel density must satisfy the condition:

$$\rho_f > \frac{10}{R_f} = \frac{10}{r_0}\left(\frac{\rho_f}{\rho_0}\right)^{\frac{1}{3}} \tag{2.12}$$

considering $\rho_0 r_0^3 = \rho_f R_f^3$. The above condition can be rewritten in the form

$$\frac{\rho_f}{\rho_0} > \left(\frac{10}{r_0 \rho_0}\right)^{\frac{3}{2}} \tag{2.13}$$

Therefore, a 2000-fold compression to the solid density enables $\rho_f R_f > 10$ g/cm^2 when the initial fuel radius $r_0 = 3$ mm.

The energy required to compress a material is equal to the internal energy of the material. Internal energy of material is defined by the Fermi energy

$$\varepsilon_F = \frac{\hbar^2}{2m_e}(3\pi^2 n_e)^{\frac{2}{3}} \tag{2.14}$$

if the temperature of the material is much less than Fermi temperature, $T_F = \varepsilon_F / k_B$. Since Fermi temperature of solid D-T fuel (18K) is around 4.9eV, solid D-T fuel is in Fermi degenerated state. Then the internal energy of a material per unit volume is given by

$$E = \frac{3}{5} n \varepsilon_F \tag{2.15}$$

where n is the density. Pressure is given by $p = nkT_{\mathrm{eq}F}$, where $T_{\mathrm{eq}F}$ is effective Fermi temperature:

$$kT_{\mathrm{eq}F} \equiv \frac{2}{5}\varepsilon_F \quad \left(\because \frac{3}{2} kT_{\mathrm{eq}F} = \frac{3}{5}\varepsilon_F\right) \tag{2.16}$$

Therefore, under the ideal isentropic compression, required energy to compress the material per unit volume is given as

$$\frac{3}{5}n_{\rm f}\varepsilon_F = \frac{3\hbar^2}{10m_e}(3\pi^2)^{\frac{2}{3}}n_{\rm f}^{\frac{5}{3}} = \frac{3\hbar^2}{10m_e}(3\pi^2)^{\frac{2}{3}}n_0^{\frac{5}{3}}\left(\frac{n_{\rm f}}{n_0}\right)^{\frac{5}{3}} \tag{2.17}$$

where n_0 and $n_{\rm f}$ are the fuel density before and after compression ($n_0 = 4.5 \times 10^{22}{\rm cm}^{-3}$). Actually isentropic compression is hardly possible and a certain degree of pre-heating occurs. Then the required energy can be described as $(3/5)\alpha n_{\rm f}\varepsilon_F$ with a pre-heating factor of $\alpha = 2$–3.

Then compression energy per unit mass $\mathcal{E}_{\rm c}$ is given by

$$\begin{aligned}\mathcal{E}_{\rm c} &= \frac{1}{\rho_{\rm f}}\frac{3}{5}\alpha n_{\rm f}\varepsilon_F = \frac{1}{\rho_{\rm f}}\frac{3\alpha\hbar^2}{10m_e}(3\pi^2)^{\frac{2}{3}}n_0^{\frac{5}{3}}\left(\frac{n_{\rm f}}{n_0}\right)^{\frac{5}{3}} = \frac{3\alpha\hbar^2}{10m_e m_i}(3\pi^2 n_0)^{\frac{2}{3}}\left(\frac{n_{\rm f}}{n_0}\right)^{\frac{2}{3}} \\ &= 1.045\times 10^5\alpha\left(\frac{n_{\rm f}}{n_0}\right)^{\frac{2}{3}}\ [{\rm J/g}].\end{aligned} \tag{2.18}$$

For example, in case of $\alpha = 3$, 4.95×10^7 J/g is needed for 2000-fold compression to the solid density.

2.1.4 Ignition and propagation burn

As described in the previous subsection, compression of the fuel enables the achievement of the areal density that can lead to fusion burn with a reasonable energy amount. However, it is not possible to induce fusion burn with only the fuel compression.

Considering the heating of the whole compressed fuel by an external energy source, the energy required to heat the fuel to 10 keV per unit mass is $\mathcal{E}_{\rm h} = 1.13 \times 10^9$ J/g. In addition, energy per unit mass $\mathcal{E}_{\rm c} = 4.95 \times 10^7$ J/g is required to compress the fuel. However, the energy released from D-T reaction per unit mass is $Q_{\rm DT} = 3.4 \times 10^{11}$ J/g. Then core gain is

$$G_{\rm f} = \frac{E_{\rm fus}}{M_{\rm DT}(\mathcal{E}_{\rm h}+\mathcal{E}_{\rm c})} = \frac{f_{\rm b}Q_{\rm DT}}{\mathcal{E}_{\rm h}+\mathcal{E}_{\rm c}}\ . \tag{2.19}$$

Then $G_{\rm f} \sim 85$ for $f_{\rm b} = 30$ % . In this case the fusion gain is only 8.5 for $\eta_{\rm h} = 0.1$, which is totally insufficient.

As described above, the energy required for compression is much less than that for heating. Thus a novel idea is considered that only small portion of the fuel is externally heated to induce fusion reaction and the remaining fuel is subsequently heated by the energy released from the fusion reaction. This process is called as "propagation burn". Let the mass in the initially heated region (called "ignitor" or "hot spot") is $M_{\rm s}$ then the required energy is described as

$$M_{\rm f}\mathcal{E}_{\rm c} + M_{\rm h}\mathcal{E}_{\rm h} \tag{2.20}$$

In this case core gain becomes

$$G_{\rm f} = \frac{Q_{\rm DT}M_{\rm f}f_{\rm b}}{M_{\rm f}\mathcal{E}_{\rm c}+M_{\rm s}\mathcal{E}_{\rm h}} = \frac{Q_{\rm DT}f_{\rm b}}{\mathcal{E}_{\rm c}+(M_{\rm s}/M_{\rm f})\mathcal{E}_{\rm h}}\ . \tag{2.21}$$

If the mass ratio in hot spot to total fuel is 5 %, the required energy for 2000-fold compression to solid density and heating the hot spot to 10 keV is about 1.1×10^8 J/g. Then core gain is around 960 for $f_\mathrm{b} = 0.3$. If $\eta_\mathrm{h} = 0.1$, fusion gain is 96, which is close to the required value.

2.1.5 Self-heating condition

Such burn propagation can be achieved when the energy deposited in the fuel is greater than that lost due to several mechanisms. Let Q_fus, Q_r, Q_c and Q_m are energy density released by fusion reaction, energy densities lost by radiation, electron heat conduction, and mechanical work, respectively (unit in $\mathrm{W/m^3}$). Then the self-heating condition can be described as

$$f_\mathrm{dep} Q_\mathrm{fus} > Q_\mathrm{r} + Q_\mathrm{c} + Q_\mathrm{m} \tag{2.22}$$

where the ratio of the energy deposited in the burning region. Here left-hand side of Eq. (2.22) is rewritten as

$$f_\mathrm{dep} Q_\mathrm{fus} = Q_\alpha (f_\alpha + 4 f_n) \tag{2.23}$$

where

$$Q_\alpha = E_{\alpha,\mathrm{DT}} n_\mathrm{s}^2 \langle \sigma v \rangle_\mathrm{s} = A_\alpha \rho_\mathrm{s}^2 \langle \sigma v \rangle_\mathrm{s} \tag{2.24}$$

is the energy density of α particles and $E_{\alpha,\mathrm{DT}}$ is the energy of α particle released from D-T reaction (3.5 MeV) . f_α and f_n are energy deposition rates of fusion-generated α particle and neutron, respectively. They are given by

$$f_\alpha = \begin{cases} \dfrac{3}{2} w - \dfrac{4}{5} w^2 & \left(w \leq \dfrac{1}{2} \right) \\ 1 - \dfrac{1}{4w} - \dfrac{1}{160 w^3} & \left(w \geq \dfrac{1}{2} \right) \end{cases} \tag{2.25}$$

$$f_n = \frac{\rho_\mathrm{s} R_\mathrm{s}}{\rho_\mathrm{s} R_\mathrm{s} + H_n} \tag{2.26}$$

where $w = R_\mathrm{s}/\lambda_{\alpha e}$ and

$$\lambda_{\alpha e} = 1.07 \times 10^4 \frac{T_\mathrm{s}[\mathrm{keV}]}{\rho_\mathrm{s} \ln \Lambda_{\alpha e}} \tag{2.27}$$

is the range of α particle in the fuel. It is known that $H_n = 20$ g/cm^2 [11]. Coulomb logarithm Λ is given by its classical value

$$\ln \Lambda = \ln \left(\frac{\sqrt{\lambda_\mathrm{D}^2 + b_\mathrm{I}^2}}{b_\mathrm{I}} \right) \tag{2.28}$$

when average distance between particles $r_\mathrm{ave} = (4\pi/3n)^{1/3}$ is larger then Bohr radius $r_\mathrm{Bohr} = \varepsilon_0 h^2 / \pi m_e e^2$. Here λ_D

$$\lambda_\mathrm{D} = \sqrt{\frac{\varepsilon_0 k T_e}{n_e e^2}} \tag{2.29}$$

is Debye length and

$$b_{\mathrm{I}} = \frac{Ze^2}{4\pi\varepsilon_0 m_{\mathrm{r}} u^2} \simeq \frac{Ze^2}{4\pi\varepsilon_0 (3/2) kT_e} \tag{2.30}$$

is impact factor. If $r_{\mathrm{ave}} < r_{\mathrm{Bohr}}$, Coulomb logarithm is approximately given by

$$\ln\Lambda = \frac{1}{2}\left\{\ln(1+\hat{\Lambda}^2) - 1\right\} \tag{2.31}$$

considering quantum mechanics effect [12]. Here

$$\hat{\Lambda} = \Lambda_{\mathrm{s}} \left\{ 0.37 + \left(\frac{T_F}{T}\right)^2 \right\}^{\frac{1}{2}} \tag{2.32}$$

$$\Lambda_{\mathrm{s}}^2 = \frac{12 m_e k T_e \lambda_{\mathrm{D}}^2}{\hbar^2} \tag{2.33}$$

If the media is optically thin and neglecting relativistic effect, radiation loss is dominated by bremsstrahlung

$$Q_{\mathrm{r}} = Q_{\mathrm{b}} = \frac{Z^2 e^6 n_e n_i \sqrt{kT_e}}{12\pi\varepsilon_0^3 c^3 m_e^{3/2} h} = A_{\mathrm{b}} \rho_{\mathrm{s}}^2 T_{\mathrm{s}}^{\frac{1}{2}} \ . \tag{2.34}$$

However, radiation cannot exceed black body radiation. Intensity of black body radiation is

$$I_{\mathrm{bb}} = \sigma_{\mathrm{B}} T_{\mathrm{s}}^4, \quad \sigma_{\mathrm{B}} = 1.03 \times 10^{17} \mathrm{J\ cm^{-2}\ s^{-1}\ keV^{-4}} \ . \tag{2.35}$$

Then radiation energy density is given by

$$Q_{\mathrm{bb}} = \frac{3\sigma T_{\mathrm{s}}^4}{R_{\mathrm{s}}} \tag{2.36}$$

since

$$\frac{4}{3}\pi R_{\mathrm{s}}^3 Q_{\mathrm{c}} = 4\pi R_{\mathrm{s}}^2 I_{\mathrm{bb}} \tag{2.37}$$

Considering this effect, radiation loss is described as

$$Q_{\mathrm{r}} = Q_{\mathrm{b}} \left(1 + \frac{Q_{\mathrm{b}}}{Q_{\mathrm{bb}}}\right)^{-1} \tag{2.38}$$

(in most application of inertial fusion, black body radiation is negligible and we can use Eq.(2.34) for the evaluation of radiation loss).

Electron heat conduction is given by

$$Q_{\mathrm{c}} = 3K_e \frac{\nabla T_{\mathrm{s}}}{R_{\mathrm{s}}} \tag{2.39}$$

here we assume the conduction energy density per unit volume is equal to the energy flux from the surface:

$$\frac{4}{3}\pi R_{\mathrm{s}}^3 Q_{\mathrm{c}} = 4\pi R_{\mathrm{s}}^2 K_e \nabla T_{\mathrm{s}} \ . \tag{2.40}$$

Here

$$K_e = 3.16\frac{n_e k T_e \tau_e}{m_e} \tag{2.41}$$

is heat conduction coefficient of electron and

$$\tau_e = \frac{\sqrt{36}\pi\varepsilon_0^2 m_e^{1/2}(kT_e)^{\frac{3}{2}}}{n_e e^4 \ln\Lambda} \tag{2.42}$$

is the momentum relaxation time of electron. Since temperature gradient at the edge of hot spot is proportional to T_s/R_s, conduction loss can be described as

$$Q_c = 3aK_e\frac{T_s}{R_s^2} = 3a\frac{A_c}{\ln\Lambda}\frac{T_s^{\frac{7}{2}}}{R_s^2} \tag{2.43}$$

where a is the proportional factor.

If the pressure of hot spot is different from that of surrounding fuel, energy density lost by mechanical work is given by

$$Q_m = \frac{3(p_s - p_f)u}{R_s} \tag{2.44}$$

where p_s, p_f and u are pressure of hot spot, pressure of cold fuel and expansion velocity of hot spot. In isochoric case, $p_s \gg p_f$ and u can be estimated by the velocity of material behind the strong plane shock $u = (3p_s/4\rho_c)^{1/2}$, respectively. Then considering isochoric state ($\rho_s = \rho_c$) and the relation $p_s \propto \rho_s T_s$, we can obtain

$$Q_m = A_m \rho_s T_s^{\frac{3}{2}} R_s^{-1} \tag{2.45}$$

Substituting Eqs. (2.23), (2.24), (2.34), (2.43) and (2.45) into Eq. (2.22), we can finally obtain the self-heating condition as a quadratic equation of $\rho_s R_s$ as

$$\left(A_\alpha f_\alpha \langle\sigma v\rangle - A_b T_s^{\frac{1}{2}}\right)(\rho_s R_s)^2 - A_m T_s^{\frac{3}{2}}(\rho_s R_s) - \frac{3a}{\ln\Lambda}A_c T_s^{\frac{7}{2}} > 0 \tag{2.46}$$

Figure 2.5 shows the self-heating condition curve on $\rho_s R_s$-T_s plane calculated from Eq. (2.46).

2.1.6 Ignition condition

The previous subsection considered an instantaneous power balance, which determines whether a hot spot with a certain parameters cools or heats. However 1-D hydrodynamic simulation indicates that ignition can also be achieved by a hot spot with its initial condition that do not satisfy the self-heating condition. The mechanism can be explained as the following. Initially the hot spot is cooled by the loss mechanisms. However, α-particles and electron conduction heat a thin layer of the surrounding cold fuel. Then a part of fuel is ablated and the mass and ρR of the hot spot increases. Then the hot spot can capture a larger fraction of α-particles and recover its energy and finally may be heated again enough to achieve ignition.

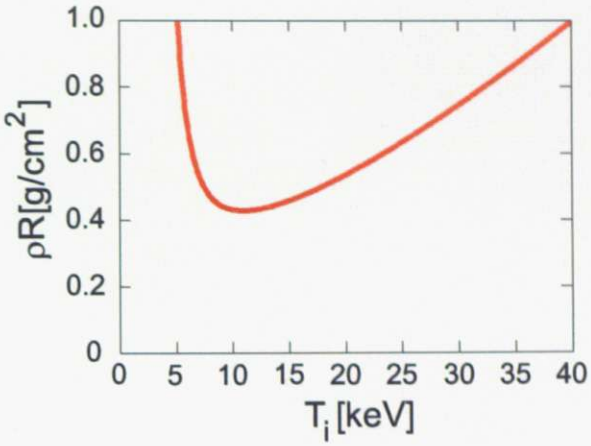

Fig. 2.5: The curve of the self-heating condition for D-T reaction on ρR-T plane

The condition of the hot spot parameters which leads to the ignition (called as "ignition condition") can be described by a simple analytical model. Energy conservation in the whole burning region is written as

$$\frac{\mathrm{d}(eM)}{\mathrm{d}t} = (Q_\alpha - Q_\mathrm{r})V - pSu\ , \tag{2.47}$$

where e, M. V, S and u are specific energy of the burning fuel, the total mass of the fuel, the volume of the fuel, the surface area of the fuel, and the velocity of the front of the burn wave, respectively. The rate of mass accretion is simply estimated by assuming that the power transmitted by the escaping α particle and electron thermal conduction just increase the specific energy of the cold material:

$$e\frac{\mathrm{d}M}{\mathrm{d}t} = \left[Q_\alpha(1-f_\alpha) + Q_\mathrm{c}\right]V, \tag{2.48}$$

where the internal energy of the fuel in front of the burn wave is assumed to be small enough compared with e for simplicity.

It is useful to rewrite Eqns. (2.47) and (2.48) in the dimensionless form. Here some notation is needed about the front velocity of the burn wave, i.e., the expansion velocity $\mathrm{d}R/\mathrm{d}t$ of the hot spot radius. A pressure imbalance between the hot spot and the surrounding fuel drives a shock wave which propagates outwards far outside the burning fuel. Then front of the hot spot advances in the already shocked fuel (ordinary deflagration process). Here the relative velocity of the burn wave with respect to the shocked material is much smaller than the velocity of the material itself u_sm, so that the expansion velocity can be approximately set to be $\mathrm{d}R/\mathrm{d}t = u_\mathrm{sm}$.

Then using the relations,

$$V = \frac{4}{3}\pi R^3, \qquad S = 4\pi R^2, \qquad M = \rho V, \tag{2.49}$$

Eq. (2.47) can be rewritten in the form

$$\rho V\frac{\mathrm{d}e}{\mathrm{d}t}+e\frac{\mathrm{d}M}{\mathrm{d}t}=\left[(Q_\alpha-Q_\mathrm{r})-\frac{3pu_\mathrm{sm}}{R}\right]V\,. \tag{2.50}$$

Then substituting Eq. (2.48) into it and using the relation

$$e=\frac{3}{2}\Gamma_B T_\mathrm{s},\qquad p=\rho\Gamma_B T_\mathrm{s} \tag{2.51}$$

and defining characteristic hydrodynamic time as $t^*=R/u_\mathrm{sm}$, Eq. (2.51) can be rewritten in the dimensionless form:

$$\frac{t^*}{T_\mathrm{s}}\frac{\mathrm{d}T_\mathrm{s}}{\mathrm{d}t}=K_\alpha f_\alpha-K_\mathrm{c}-K_\mathrm{r}-2 \tag{2.52}$$

where K_α, K_c, K_r are the dimensionless power density

$$K_\alpha=\frac{t^*}{\rho e}Q_\alpha,\qquad K_\mathrm{c}=\frac{t^*}{\rho e}Q_\mathrm{c},\qquad K_\mathrm{r}=\frac{t^*}{\rho e}Q_\mathrm{r}\,. \tag{2.53}$$

In what follows, we omit subscript 's' for simplicity. Similarly, Eq. (2.48) can be reduced in the form

$$\frac{t^*}{\rho}\frac{\mathrm{d}\rho}{\mathrm{d}t}=K_\alpha(1-f_\alpha)+K_\mathrm{c}-3\,. \tag{2.54}$$

Here instructive result is obtained by using the strong shock limit for the expression of u_sm;

$$u_\mathrm{sm}\simeq\sqrt{\frac{3p}{4\rho_\mathrm{c}}}=\sqrt{\frac{3\rho\Gamma_B T_\mathrm{h}}{4\rho_\mathrm{c}}}=\sqrt{\frac{\rho e}{2\rho_\mathrm{c}}}\,, \tag{2.55}$$

and taking the approximate expression of the fusion reactivity in temperature power law as $\langle\sigma v\rangle\propto T_\mathrm{h}^m$. Then characteristic hydrodynamic time is rewritten in the form

$$t^*=\frac{\sqrt{2}R}{\sqrt{e}}\sqrt{\frac{\rho_\mathrm{c}}{\rho}}\,, \tag{2.56}$$

and dimensionless alpha heating power density becomes

$$K_\alpha=\frac{R\sqrt{2\rho_\mathrm{c}}}{(\rho e)^{\frac{3}{2}}}\rho^2T^m\,. \tag{2.57}$$

Here taking time derivative of Eq. (2.57), we can obtain the relation

$$\frac{t^*}{K_\alpha}\frac{\mathrm{d}K_\alpha}{\mathrm{d}t}=\frac{1}{2}\frac{t^*}{\rho}\frac{\mathrm{d}\rho}{\mathrm{d}t}+\left(m-\frac{3}{2}\right)\frac{t^*}{T}\frac{\mathrm{d}T}{\mathrm{d}t}+1\,. \tag{2.58}$$

Substituting eqns (2.53) and (2.54) into Eq. (2.58), it is found that

$$\frac{t^*}{K_\alpha}\frac{\mathrm{d}K_\alpha}{\mathrm{d}t}=\frac{1+2(m-2)f_\alpha}{2}K_\alpha-(m-2)K_\mathrm{c}-\frac{2m-3}{2}K_\mathrm{r}+\frac{5}{2}-2m\,. \tag{2.59}$$

If $m\approx 2$, Eq. (2.59) is reduced to the simple form;

$$\frac{t^*}{K_\alpha}\frac{\mathrm{d}K_\alpha}{\mathrm{d}t}=\frac{1}{2}(K_\alpha-K_\mathrm{r}-3)\,. \tag{2.60}$$

If the right-hand side of Eq. (2.60) is greater than zero, alpha heating power grows. This condition coincides to the inequality

$$(Q_\alpha - Q_\mathrm{r})t_0^* > 3\rho e = \frac{9}{2}\rho\Gamma_B T \ . \tag{2.61}$$

Then substituting Eqns. (2.24) and (2.38) into this equation, finally we find the ignition condition in the similar form as the Lawson condition of magnetic confinement fusion;

$$\rho_\mathrm{s} R_\mathrm{s} T_\mathrm{s} > \frac{9\sqrt{3}}{4}\frac{\Gamma_B^{\frac{3}{2}} T_\mathrm{s}^{\frac{5}{2}}}{A_\alpha\langle\sigma v\rangle - A_\mathrm{b} T_\mathrm{s}^{\frac{1}{2}}}\left(\frac{\rho_\mathrm{s}}{\rho_\mathrm{c}}\right)^{\frac{1}{2}} \ . \tag{2.62}$$

Then it is found that higher core density lowers the required fusion triple products. This fact become quite important in the fast ignition scheme to reduce heating energy.

2.2 Implosion and central ignition

2.2.1 Central ignition

As described in the previous section, high gain achievement in inertial fusion requires:

- isentropic compression of the most of the fuel
- creation of the hot spot (the region where satisfies ignition condition) in the portion of the fuel

After numerous theoretical and numerical studies, it is shown that a relatively weak initial shock introduced into an otherwise isentropic hollow-shell implosion can achieve both conditions given in the above [13]. This scheme is called as "central-ignition". The physics related isentropic compression of the hollow spherical shell is reviewed in section 4.3. Here we briefly review the estimation of the fusion gain by the central ignition scheme.

In case of the central ignition, the entire fuel (including hot spot and surrounding cold fuel) satisfies the pressure equilibrium, and then hot spot becomes high temperature and low density, whereas surrounding fuel becomes low temperature and high density. The internal energy of the fuel is given by

$$E_\mathrm{f} = 3n_\mathrm{s}kT_\mathrm{s}V_\mathrm{s} + \frac{3}{5}\alpha\varepsilon_F n_\mathrm{c} V_\mathrm{c} \tag{2.63}$$

where V is the volume of the fuel and subscripts s, c, f denotes the variables is related to hot spot, surrounding cold fuel, the entire compressed fuel, respectively. In Eq. (2.63), n, T are the density and temperature of the ion and assuming charge neutrality $n_i = n_e$ (here $Z = 1$) and isothermal condition $T_i = T_e$, then $(3/2)(n_i kT_i + n_e kT_e) = 3nkT$. By using the relation of pressure equilibrium $n_\mathrm{s}kT_\mathrm{s} = (2/5)\alpha\varepsilon_F n_\mathrm{c}$, Eq. (2.63) can reduced into

$$E_\mathrm{f} = \frac{3}{5}\alpha\varepsilon_F n_\mathrm{c} V_\mathrm{f} \ . \tag{2.64}$$

In case of the central ignition, the burning time can be estimated by

$$\tau_{\rm b} = \frac{R_{\rm f} - R_{\rm s}}{c_{\rm sc}} \ , \tag{2.65}$$

where $c_{\rm sc}$ is the sound velocity in the cold fuel. Then the burn fraction estimated by Eq. (2.11) is described by

$$f_{\rm b} = \frac{\rho_{\rm c}(R_{\rm f} - R_{\rm s})}{\tilde{\beta}(T) + \rho_{\rm c}(R_{\rm f} - R_{\rm s})} \ , \tag{2.66}$$

where

$$\tilde{\beta}(T) = \frac{2m_i c_{\rm sc}}{\langle \sigma v \rangle} \ . \tag{2.67}$$

Neglecting the contribution from the hot spot, the fusion power is given by

$$E_{\rm fus} = n_{\rm c} m_i V_{\rm c} Q_{\rm DT} f_{\rm b} \ , \tag{2.68}$$

and then core gain is obtained as

$$G_{\rm f} \sim \frac{5 m_i Q_{\rm DT}}{3\alpha\varepsilon_F} \frac{V_{\rm c}}{V_{\rm f}} \frac{\rho_{\rm c}(R_{\rm f} - R_{\rm s})}{\tilde{\beta}(T) + \rho_{\rm c}(R_{\rm f} - R_{\rm s})} \ . \tag{2.69}$$

Considering 2000-fold compression to the solid density ($\rho_{\rm c} = \rho_{\rm DT,solid} = 420$ g/cm^3), Fermi energy is $\varepsilon_F = 786$ eV. Assuming $T_{\rm s} = 5$keV and $\alpha = 2$, the density of the hot spot is $\rho_{\rm s} = \alpha\varepsilon_F \rho_{\rm c}/5kT_{\rm s} = 27.2$ g/cm^3. According to the result obtained in the previous subsection, self-heating condition requires $\rho_{\rm s} R_{\rm s} \geq 0.4$ g/cm^2 for $T_{\rm s} = 5$ keV, then $R_{\rm s} = 0.015$ cm. The cold fuel temperature estimated by the pressure equilibrium condition $5n_{\rm s}\varepsilon_F/\alpha n_{\rm c}$ is $T_{\rm c} = 810$ eV, and by using Eq. (2.67) then we obtain $\tilde{\beta}(T) = 10.9$ g/cm^2. If assuming $R_{\rm f} = 0.03$ cm, core gain is $G_{\rm f} = 3086$ and fusion gain of $G = 310$ is expected with $\eta_{\rm h} = 0.1$.

2.2.2 Mechanism of implosion and required ablation pressure

In case of central ignition, the conversion efficiency from injection energy to the internal energy of the fuel is the product of the absorption coefficient of injection energy to the ablator $\eta_{\rm ab}$, hydrodynamic efficiency (conversion efficiency from the energy of ablator to the kinetic energy of the fuel shell) $\eta_{\rm hydro}$, and transformation efficiency (conversion efficiency from the fuel kinetic energy to the internal energy) $\eta_{\rm tr}$:

$$\eta_{\rm c} = \eta_{\rm ab}\eta_{\rm hydro}\eta_{\rm tr} \ . \tag{2.70}$$

If assuming pre-heating factor $\alpha = 3$, Eq. (2.18) shows the internal energy per unit mass of the fuel compressed to 1000-fold to the solid density $\mathcal{E}_{\rm c} \sim 3 \times 10^{10}$ J/kg. This energy coincides to the kinetic energy with the velocity $V = 2.5 \times 10^5$ m/s if assuming $\mathcal{E}_{\rm c} = V^2/2$. Then if accelerated fuel has the velocity of this order, 1000-fold compression to the solid density is possible.

The shell implosion with steady state energy deposition can be modeled as described in figure 2.6 [14]. Here ablation surface is the surface of the solid fuel shell, and Chapman-Jouguet (C-J) point is the one at which flow velocity of the ablated plasma is equal to the sound velocity. The plasma outside C-J point expands isothermally. Let M, R, V are the mass, radius and velocity of the imploded shell, $P_{\rm a}$, $P_{\rm C\text{-}J}$ are the pressure at the ablation surface, at the C-J point, and u is the velocity of expanding plasma, respectively, Since the flow velocity outside the C-J point exceeds sound velocity, pressure perturbation

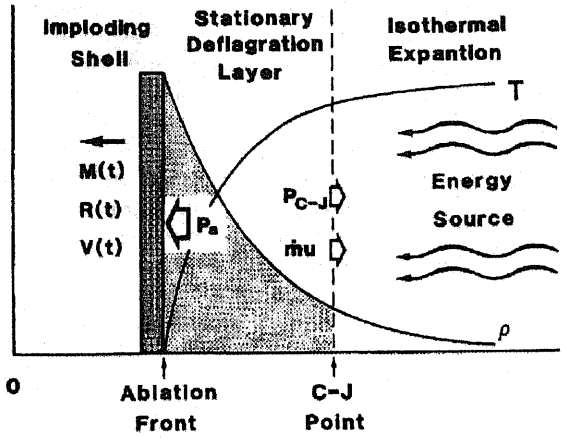

Fig. 2.6: Schematic view of the model for the implosion of spherical shell pellet with steady-state energy injection (Fig. 1 of reference [14])

in the blow-off plasma cannot affect the region within the C-J point. Thus pressure transmitted to the ablation surface can be described as $P_{\rm a} - P_{\rm C\text{-}J}$ and the equation of motion is given by

$$\frac{{\rm d}(MV)}{{\rm d}t} - (u+V)\frac{{\rm d}M}{{\rm d}t} = -4\pi R^2(P_{\rm a} - P_{\rm C\text{-}J}) \ . \tag{2.71}$$

Here

$$\frac{{\rm d}M}{{\rm d}t} = 4\pi R^2 \dot{m} \tag{2.72}$$

and

$$\dot{m}u \simeq \rho_{\rm C\text{-}J} c_{\rm s}^2 \simeq P_{\rm C\text{-}J} \ , \tag{2.73}$$

then Eq. (2.71) can also be written in the form;

$$M\frac{{\rm d}V}{{\rm d}t} = -4\pi R^2 P_{\rm a} \ . \tag{2.74}$$

Assuming the ablation pressure is a constant and the mass of ablator is much smaller than the total mass of the fuel, it is found that $M \approx M_0 = 4\pi\rho_0 R_0^2 \Delta R_0$ (ΔR is the thickness of the fuel shell and subscript '0' denotes the value is the one at the initial state, i.e., before the implosion). Then by using

Eq. (2.74), we can find

$$\frac{\mathrm{d}V}{\mathrm{d}t} = -\frac{4\pi P_{\mathrm{a}}}{M_0}R^2 = -\frac{P_{\mathrm{a}}}{\rho_0 R_0^2 \Delta R_0}R^2 \ . \tag{2.75}$$

Multiplying Eq. (2.75) by $V = \dfrac{\mathrm{d}R}{\mathrm{d}t}$ and integrating it, we find

$$\frac{1}{2}V^2 = -\frac{P_{\mathrm{a}}}{\rho_0 R_0^2 \Delta R_0}\frac{1}{3}(R^3 - R_0^3) \ . \tag{2.76}$$

Since $R \sim 0.1R_0$, and $R^3 \ll R_0^3$ then ablation pressure can be given by

$$P_{\mathrm{a}} = \frac{3}{2}\rho_0 V^2 \frac{\Delta R_0}{R_0} \ . \tag{2.77}$$

Then it is found that required ablation pressure can be reduced if the initial fuel aspect ratio, the ratio of the initial fuel inner radius to the initial shell thickness, becomes larger. For example, the required ablation pressure to obtain the velocity $V = 3 \times 10^5$ m/s is $P_{\mathrm{a}} = 4.5 \times 10^{12}$ Pa for $A_0 = 30$, $\rho_0 = 1\mathrm{g/cm}^3$ [1)].

2.2.3 Required energy intensity for implosion

According to the model given in the previous section, the absorbed driver energy is consumed as the kinetic energy E_{ek} and the internal energy E_{ei} of expanding plasma at the C-J point, the energy of isothermal expanding plasma E_{iso}, and the ionization energy to produce plasma E_{ion}. Let $\hat{}$ denotes the quantities per unit area, we can obtain

$$\hat{E_{\mathrm{ek}}} = \frac{1}{2}\dot{m}u^2 \simeq \frac{1}{2}\rho_{\text{C-J}}c_{\mathrm{s}}^3 \tag{2.78}$$

$$\hat{E_{\mathrm{ei}}} = \frac{P_{\text{C-J}}}{(\gamma-1)\rho_{\text{C-J}}}\dot{m} \simeq \frac{3}{2}\rho_{\text{C-J}}c_{\mathrm{s}}^3 \tag{2.79}$$

$$\hat{E_{\mathrm{iso}}} = P_{\text{C-J}} \simeq \rho_{\text{C-J}}c_{\mathrm{s}}^3 \tag{2.80}$$

here the relation $\gamma = 5/3$ is used.

For simplicity, ionization energy is regarded as zero. Then the intensity of injected laser energy I_{d} is given as the sum of the above three energies;

$$\eta_{\mathrm{ab}} I_{\mathrm{d}} = E_{\mathrm{ek}} + E_{\mathrm{ei}} + E_{\mathrm{iso}} = 3\rho_{\text{C-J}}c_{\mathrm{s}}^3 \tag{2.81}$$

where η_{ab} is the absorption efficiency of the injected energy to the ablation layer. Generally the pressure at the ablation front is 1.2 to 2 times larger than that at C-J point. But here we assume they are equal to each other ($P_{\mathrm{a}} \sim P_{\text{C-J}} \simeq \rho_{\text{C-J}}c_{\mathrm{s}}^2$) for simplicity. Then we obtain the relations

$$\eta_{\mathrm{ab}} I_{\mathrm{d}} \simeq 3\rho_{\text{C-J}}\left(\frac{P_{\mathrm{a}}}{\rho_{\text{C-J}}}\right)^{\frac{3}{2}} \tag{2.82}$$

[1)] Since ρ_0 in this equation includes the contribution from the mass of the ablator, it is larger than the solid density of D-T fuel (=0.21 g/cm^3).

and

$$P_{\mathrm{a}} \simeq \left(\frac{\rho_{\text{C-J}}^{\frac{1}{2}} \eta_{\mathrm{ab}} I_{\mathrm{d}}}{3} \right)^{\frac{2}{3}} \tag{2.83}$$

In case of laser driver, the energy of laser is absorbed at the outer region from the cut-off surface and transmitted to inner region by thermal conduction. Generally the density of C-J point can be a few to ten times larger than the cut-off density. But here we also they are equal to each other for simplicity [2)]. Then we obtain

$$\rho_{\text{C-J}} = \rho_{\mathrm{c}} = m_i n_{\mathrm{c}} = m_i \frac{m_e \varepsilon_0}{Ze^2} \omega_{pe}^2 = m_i \frac{m_e \varepsilon_0}{Ze^2} \left(\frac{2\pi c}{\lambda} \right)^2 . \tag{2.84}$$

Substituting this into Eq. (2.83) yields

$$P_{\mathrm{a}} = \left(\frac{2\pi c (\varepsilon_0 m_e m_i)^{\frac{1}{2}} \eta_{\mathrm{ab}} I_{\mathrm{d}}}{3eZ^{\frac{1}{2}} \lambda} \right)^{\frac{2}{3}} . \tag{2.85}$$

In case of D-T fuel, $m_i = 2.5 \times 1.67 \times 10^{-27} \mathrm{kg/m^3}$, $Z = 1$ and then we can obtain

$$P_{\mathrm{a}}[10^{12}\mathrm{Pa}] = 0.803 \left(\frac{(\eta_{\mathrm{ab}} I_{\mathrm{d}})[10^{14}\mathrm{W/cm^2}]}{\lambda[\mu\mathrm{m}]} \right)^{\frac{2}{3}} . \tag{2.86}$$

2.2.4 Absorption efficiency of injected energy to ablator

According to the result obtained in the previous subsection, it is required to achieve high absorption efficiency η_{ab} to obtain high ablation pressure.

The injection energy is absorbed by ablation layer through the following three basic processes

(a) inverse bremsstrahlung

(b) resonance absorption

(c) parametric process

It is known that η_{ab} increases with decreasing wavelength and intensity of the laser. Experimentally absorption coefficient of 80–90 % is achieved with blue laser light with wavelength $\lambda = 0.35$ μm and the intensity range over 10^{14}–10^{15} W/cm^2. If this level of η_{ab} is achieved, the required laser intensity is 6.9×10^{14} W/cm^2 to satisfy ablation pressure estimated by Eq. (2.86), i.e., 4.5×10^{12} Pa. Assuming the initial radius of the fuel pellet to be 1 mm, the surface area is about 0.1 cm^2. Then the required implosion energy is the order of 1 MJ since the time used for the implosion is the order of 10 nsec.

[2)] This simplification gives fairly good approximation. The final result (Eq. (2.85)) differs only 2.15 times of the true value if the actual density at C-J point is ten times of the cut-off density because it includes the term proportional to the 1/3 power of the mass density.

2.2.5 Hydrodynamic efficiency

By using Eq. (2.74) and a parameter

$$\chi = \frac{P_{\rm a}}{\dot{m}u} \simeq \frac{P_{\rm a}}{P_{\rm C\text{-}J}} \,, \tag{2.87}$$

the velocity of imploded fuel shell is described as

$$V = \chi u \ln \tilde{M} \tag{2.88}$$

where $\tilde{M} = M/M_0$. Then the kinetic energy of imploded shell $E_{\rm sk}$ is obtained as

$$E_{\rm sk} = \frac{1}{2}MV^2 = \frac{1}{2}\chi^2 M u^2 \ln^2 \tilde{M} \,. \tag{2.89}$$

While as described in section 2.2.3, injected driver energy is equal to the sum of kinetic energy $E_{\rm ek}$, internal energy $E_{\rm ei}$ and isothermal expansion energy $E_{\rm iso}$ of ablated plasma and ionization energy $E_{\rm ion}$. Here let $\Delta M = M_0 - M$, the kinetic energy of ablated plasma is given by

$$E_{\rm ek} = \frac{1}{2}\int_0^{\Delta M} (V+u)^2 \,{\rm d}(\Delta M) \tag{2.90}$$

$$= \frac{1}{2}\int_0^{\Delta M} (\chi u \ln \tilde{M} + u)^2 \,{\rm d}(\Delta M) \tag{2.91}$$

$$= \frac{1}{2}\int_0^{\Delta M} \left\{ u^2 + 2\chi u^2 \ln\left(1 - \frac{\Delta M}{M_0}\right) + \chi^2 u^2 \ln^2\left(1 - \frac{\Delta M}{M_0}\right) \right\} {\rm d}(\Delta M) \,. \tag{2.92}$$

Here using the relation

$$\int \ln(1-ax)\,{\rm d}x = \frac{1}{a}\left\{(1-ax) - (1-ax)\ln(1-ax)\right\} \tag{2.93}$$

$$\int \ln^2(1-ax)\,{\rm d}x = -\frac{1}{a}\left[(1-ax)\ln^2(1-ax) + 2\left\{(1-ax) - (1-ax)\ln(1-ax)\right\}\right] \tag{2.94}$$

Eq. (2.92) can be reduced to the form

$$E_{\rm ek} = \Delta M u^2 \left(\chi^2 - \chi + \frac{1}{2}\right) + M u^2 \left(\chi^2 - \chi - \frac{1}{2}\chi^2 \ln \tilde{M}\right) \ln \tilde{M} \,. \tag{2.95}$$

The internal energy and expanding energy are written as

$$E_{\rm ei} = \frac{P_{\rm C\text{-}J}}{(\gamma-1)\rho_{\rm C\text{-}J}} \Delta M = \frac{3}{2}\Delta M u^2 \tag{2.96}$$

$$E_{\rm iso} = \int_\infty^R 4\pi r^2 P(r)\,{\rm d}r = u^2 \int_\infty^R 4\pi r^2 \rho(r)\,{\rm d}r = \Delta M u^2 \tag{2.97}$$

here using the relation $P(r) = \rho(r)u^2 = \rho(r)c_{\rm s}^2$. Considering charge neutrality ($n_e = Zn_i$) and isothermal condition ($T_e = T_i = T$),

$$P = \rho u^2 = n_e k T_e + n_i k T_i = (Z+1) n_i k T \simeq (Z+1)\rho \frac{kT}{m_i} \,. \tag{2.98}$$

Considering the relation

$$T \simeq \frac{m_i u^2}{Z+1} \tag{2.99}$$

and estimating ionization potential most simply as $Z^2 I_{\rm H}$ ($I_{\rm H}$ is the first ionization energy of hydrogen: 13.6 eV), the ionization energy is written in the form;

$$E_{\rm ion} = \frac{\Delta M}{m_i} \sum_{Z=1}^{Z} Z^2 I_{\rm H} = \frac{Z(2Z+1) I_{\rm H}}{6T} \Delta M u^2 \simeq \frac{Z^2 I_{\rm H}}{3T} \Delta M u^2 \ . \tag{2.100}$$

Then hydrodynamic efficiency $\eta_{\rm hydro}$ is given by

$$\eta_{\rm hydro} = \frac{E_{\rm sk}}{E_{\rm sk} + E_{\rm ek} + E_{\rm ei} + E_{\rm iso} + E_{\rm ion}} = \frac{\frac{1}{2}\chi^2 \tilde{M} \ln^2 \tilde{M}}{\left(\chi^2 - \chi + 3 + \frac{Z^2 I_{\rm H}}{3T}\right) \Delta\tilde{M} + (\chi^2 - \chi)\tilde{M} \ln \tilde{M}} \ . \tag{2.101}$$

The relation between hydrodynamic efficiency and the ablated mass ratio calculated by Eq. (2.101) is shown in figure 2.7 and 2.8. Figure 2.7 shows the relation with $\chi \simeq P_{\rm a}/P_{\rm C\text{-}J} = 1.5$ and the four cases for the coefficient of ionization energy $ZI_{\rm H}/3T = 0$, 1, 2, 3. Figure 2.8 shows the case for $\chi = 0.5$, 1.0, 1.5, 2,0 with $ZI_{\rm H}/3T = 0$. It is found that hydrodynamic efficiency $\eta_{\rm hydro}$ has its maximum at the ablated mass ratio $\Delta M/M_0 \approx 0.77$ and the maximum value of about 21 % for $\chi = 1.5$.

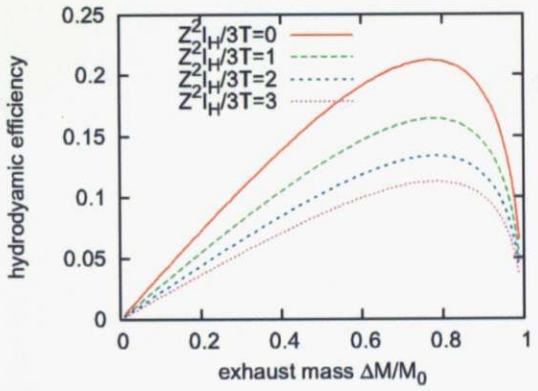

Fig. 2.7: Relation between hydrodynamic efficiency and the mass ablation ratio (dependence on ionization energy)

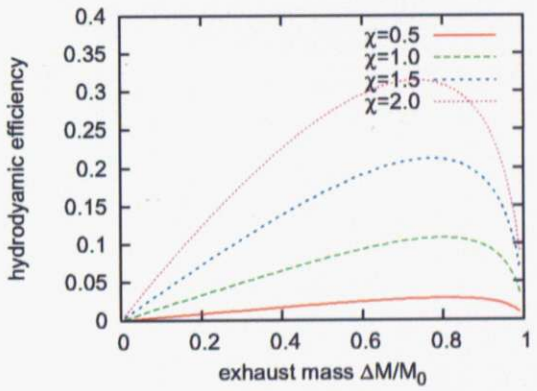

Fig. 2.8: Relation between hydrodynamic efficiency and the mass ablation ratio (dependence on pressure ratio)

From the Eq. (2.72), we find

$$\frac{\mathrm{d}M}{\mathrm{d}t} V = -4\pi \dot{m} R \frac{\mathrm{d}R}{\mathrm{d}t} \tag{2.102}$$

by using $V = \dfrac{\mathrm{d}R}{\mathrm{d}t}$. Then substituting Eq. (2.88) into this and using the relation

$$\int \frac{\mathrm{d}M}{\mathrm{d}t} \ln M \, \mathrm{d}t = M \ln M - M \tag{2.103}$$

yields

$$M\left(\ln \tilde{M} - 1\right) + M_0 = \frac{4\pi \dot{m}}{3\chi u} \left(R_0^3 - R^3\right) \ . \tag{2.104}$$

Here using the relation $M_0 = 4\pi R_0^2 \rho_0 \Delta_0$ we can obtain

$$M\left(\ln \tilde{M} - 1\right) = 1 - \frac{1}{3}\alpha\left(1 - \tilde{R}^3\right) \tag{2.105}$$

where $\tilde{R} = R/R_0$ and α is implosion parameter

$$\alpha = \frac{\dot{m} R_0}{\rho_0 \chi u \Delta_0} = \frac{P_{\text{C-J}}}{P_{\text{a}}} \frac{\rho_{\text{C-J}}}{\rho_0} A_0 \ . \tag{2.106}$$

Figure 2.9 shows the dependence on ablation parameter of the relation between fuel conversion ratio and mass ablation ratio. Then we can find entire fuel is ablated if $\alpha \geq 3$. Figure 2.10 show the relation between hydrodynamic efficiency and implosion parameter α for $\chi = 1.5$. In this case $\alpha = 1.3$ gives maximum hydrodynamic efficiency. Then generally initial aspect ratio of the pellet A_0 is limited as $3 < A_0 < 10$.

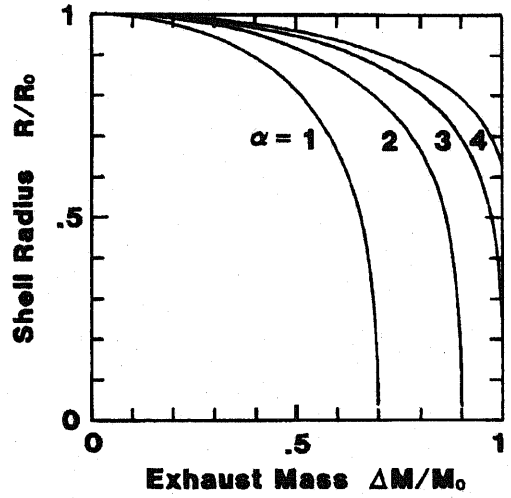

Fig. 2.9: The relation between fuel convergence ratio and mass ablation ratio (Fig. 2 of reference [14])

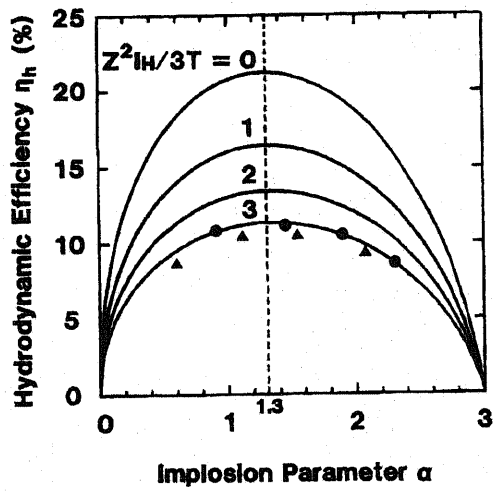

Fig. 2.10: Dependence of the relation between hydrodynamic efficiency and mass ablation ration on implosion parameter (Fig. 6 of reference [14])

2.2.6 Transformation efficiency

Although it has not become clear about the detailed physics mechanism in the conversion of hydrodynamic energy into the internal energy, numerical simulations indicates the transformation efficiency η_{tr} is proportional to the initial aspect ratio of the fuel and increase with the gas pressure in the fuel. It has little dependence on the other parameters (e.g., irradiation intensity or pellet size).

As shown in figure 2.11, expected transformation efficient is 10 % for initial gas pressure of 5 atm and 20 % for 20 atm if the initial aspect ratio is 10. In case of the initial aspect ratio is 3, it is expected to be 20 % for 5 atm and 70 % for 20 atm.

Then coupling efficiency of injected laser energy to the internal energy of compressed fuel is expected to be 12.6 % at maximum. Thus fusion gain of $G = 300$ estimated in section 2.2.1 is achievable.

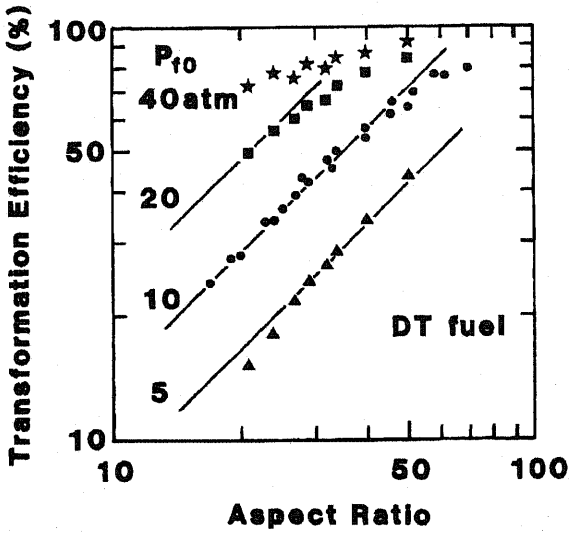

Fig. 2.11: Transformation efficiency from hydrodynamic energy into internal energy (Fig. 13 of reference [14])

2.3 Hydrodynamic instability and irradiation uniformity

2.3.1 Rayleigh-Taylor instability

Considering the state in which two immiscible fluids of different densities are in contact with each other and subjected to gravity $\boldsymbol{g}$. If the upper fluid is heavier than the lower one, the tiny perturbation generated on the interface grows exponentially in time. This instability is called as Rayleigh-Taylor (R-T) instability. R-T instability also occurs when the lighter fluid accelerates a layer of the denser fluid with the acceleration $\boldsymbol{a}$. That is because the fluid feels an inertial force per unit mass $\boldsymbol{g} = -\boldsymbol{a}$ in a frame moving with the interface.

Thus R-T instability occurs at two stages of the implosion of a fuel pellet. In the initial phase of implosion, low density, high pressure ablated plasma accelerates the high density fuel shell. Then R-T instability is occurred around the ablation surface. In the final phase of implosion, low density, high pressure hot spot decelerates the surrounding fuel and the interface is also unstable. The R-T instability can cause the mixing of cold fuel and hot ablated plasma at the acceleration phase, resulting in the increase of entropy in the cold fuel that leads to the poor compression or the collapse of the fuel. At the stagnation phase it can cause the mixing of high temperature hot spot and surrounding cold fuel and may disable ignition.

It is observed by experiments that R-T instability first grows linearly and then non-linear mode (bubble and spike) evolves. There is a well-known formula, Takabe's formula, for the linear growth rate of R-T instability at ablation with finite density scale length [15]:

$$\gamma = \gamma_0 - \beta k u_a, \qquad \gamma_0 = \sqrt{\frac{A_t k a}{1 + k L_{\min}}}\,, \tag{2.107}$$

where k, a, and $L_{\min}$ are the wave number of the unstable mode, acceleration, and minimum density scale length, respectively, and $A_t = (\rho_H - \rho_L)/(\rho_H + \rho_L)$ is Atwood number (ρ_H, ρ_L are the density of heavier and lighter material). The ablation velocity u_a is defined with mass ablation rate $\dot{m}$ and the density at ablation surface ρ_a as

$$\dot{m} = \rho_a u_a\,. \tag{2.108}$$

The first term in Eq. (2.107) is the linear growth rate with the correction of finite density scale effect, and the second term represents the stabilizing effect by the flow. Equation (2.107) is in fairly good agreement with experiments and linear growth rate of R-T instability can be estimated by this formula. More detailed description about this formula is given in chapter 4.

The linear growth of R-T instability for isolated single-mode perturbation is saturated when the perturbation velocity predicted by linear theory is equal to the asymptotic bubble velocity and then non-linear evolution is developed. There is a sophisticated theory dealing with this nonlinear evolution of single-mode perturbation. When there exists multi-mode perturbations, the phenomena becomes significantly complicated. At the earlier stage, these modes are coexists, and then mode coupling and bubble competition is occurred. Then small bubbles are washed downstream, while large bubbles run through the target. At the later stage of evolution, large structures appear and dominate the flow and flow patterns become more and more complex and chaotic. This process is called as "turbulent mixing".

One of the trigger of the R-T instability is considered to be Richtmeyer-Meshkov (R-M) instability. R-M instability occurs when the density gradient is not parallel to the pressure gradient. That corresponds the case that a shock wave passes the perturbed discontinuous plane or a perturbed shock wave passes the discontinuous plane and can be described as the following [16].

The equation of motion of ideal fluid is written as

$$\frac{\mathrm{d}\boldsymbol{u}}{\mathrm{d}t} = -\frac{1}{\rho}\nabla p\,. \tag{2.109}$$

Let $\boldsymbol{w} = \nabla \times \boldsymbol{u}$ is vortex of the flow and taking the curl of the above equation, we find

$$\frac{\mathrm{d}\boldsymbol{w}}{\mathrm{d}t} = (\boldsymbol{w}\cdot\nabla)\boldsymbol{u} - \boldsymbol{w}(\nabla\cdot\boldsymbol{u}) + \frac{1}{\rho^2}\nabla\rho\times\nabla p\,. \tag{2.110}$$

R-M instability is originate from the third term of Eq. (2.110) and it generates when perturbation exists on the discontinuous plane of density or pressure, regardless their direction (see Fig. 2.12). Here if a shock wave passes through the region where the high density region slightly swells to the low density region, the vortex excited by R-M instability can be a trigger of R-T instability (Fig. 2.13).

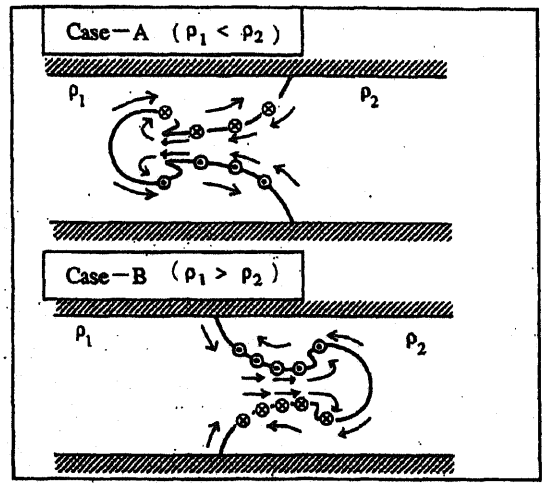

Fig. 2.12: Schematic view of growth of Richtmeyer-Meshkov instability (Fig. 8 of reference [16])

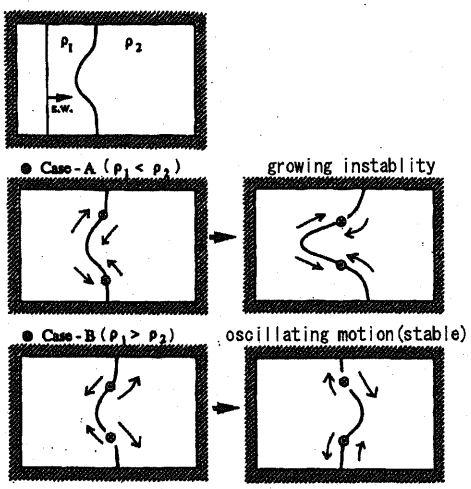

Fig. 2.13: Schematic view of growth of Rayleigh-Taylor instability (Fig. 9 of reference [16])

2.3.2 Requirement to suppress Rayleigh-Taylor instability

As mentioned in the previous subsection, R-T instability is caused by a fluctuation of the density discontinuous plane on the pellet surface and a fluctuation of ablation pressure due to the non-uniformity of irradiation energy.

As described in detail in chapter 4, the former affects the possible pellet design and laser pulse shaping. Irradiation non-uniformity is caused by:

(1) limited beam number and accuracy of alignment

(2) error in the target tracking

(3) beam misfocusing

(4) inhomogeneity in the energy and power of each beam

(5) spatial inhomogeneity in intensity due to radial intensity profile of each beam

Among them (5) leads to instability with a large wave number, the rest leads to instability with a small wave number.

Figure 2.14 (b) shows the calculation result of the relation

between beam number and irradiation non-uniformity with assumption that the beam intensity profile is perfectly parabolic. As you can see the irradiation non-uniformity strongly depends on a focus ratio (the ratio of laser radius to target radius, see Fig. 2.14 (a)). If the focus ratio is close to unity, the sufficient uniformity can be obtained with about 30 beams. The critical surface, however, shrunk inner radial direction during the implosion and focus ratio necessarily increases to about 1.8. Then about 60 beams is required to high gain target design (in case of the fast ignition, the number of beams can be reduced around 30).

Instability with small mode number can be controlled by a smoothing effect due to electron thermal conduction or optimization in the design of target and driver system. Irregularity in the energy deposition profile due to an error in the phase and amplitude of the laser beam leads the large mode number non-uniformity. This large wave number mode should be noted because it can vary its amplitude and phase during ablation and leads to Rayleigh-Taylor instability. To suppress this non-uniformity improvement in beam quality is needed.

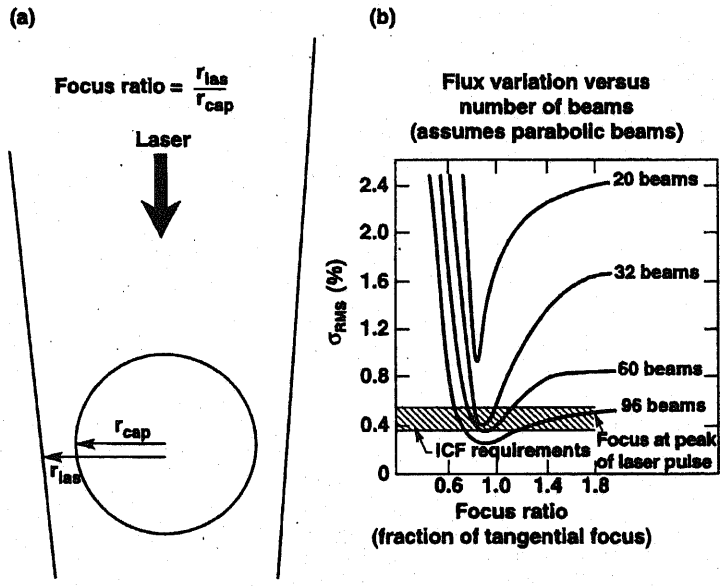

Fig. 2.14: Dependence of irradiation uniformity on focusing ratio and beam number (FIG. 2.9 of reference [17])

2.4 Fast ignition

In central ignition method, fuel pellet is imploded with keeping pressure equilibrium between accelerated cold fuel and compressed rarefied gas . Then the density of the hot spot is much lower than that of surrounding cold fuel. If it is possible to produce a hot spot in the dense region, hot spot radius to satisfy ignition condition can be reduced. Then total mass of the fuel can be also significantly reduced Then the outer radius of compressed fuel R_f to achieve sufficient ρr value for high burn fraction can be reduced and the total mass of the fuel M_f, which is roughly proportional to the required injection energy for implosion, can be also significantly reduce because $M_f \propto R_f^3$.

The idea to create hot spot by using an external heating source was proposed already in early 1980s by Dr. Yamanaka in Osaka University. The outline of this idea includes following three processes:

- First, create extremely dense fuel core by the implosion as the central ignition scheme.
- Next, create a hole in the ablated plasma corona surrounding dense core by pondermotive force of ultra intense laser and push the critical surface into near the center of the dense core.
- Finally, create a hot spot by fast electrons generated through the relativistic interaction between intense laser and the dense plasma.

If this novel idea becomes possible, several merits is brought in;

- the processes of implosion and ignition can be separated and then the difficulties accompanying the implosion process and the technological requirements to conquer it can be significantly relaxed.
- the total driver efficiency can be improved if the efficiency of ultra intense laser is high.
- the required energy for implosion can be reduced and ignition becomes possible with smaller driver energy.

Here we try to estimate the energy required for the fast ignition. It is the same as the central ignition that the creation of hot spot with $T_s = 5$ keV, $\rho_s R_s \sim 0.4\text{g/cm}^2$. The energy required to heating is given by

$$E_h = M_s \mathcal{E}_h = \frac{4}{3}\pi \rho_s R_s^3 \mathcal{E}_h = 4\pi \frac{(\rho_s R_s)^3}{3\rho_s^2} \mathcal{E}_h = 1.51 \times 10^8 \frac{1}{\rho_s^2} \text{ [J]}. \tag{2.111}$$

While the energy required to implode the fuel is given in Eq. (2.18) as

$$1.05 \times 10^5 \alpha \left(\frac{\rho_f}{\rho_0}\right) M_f \text{ [J]}. \tag{2.112}$$

Assuming isochoric state of the compressed fuel, i.e., $\rho_{\rm f} = \rho_{\rm s} = \rho$, the total energy of the fuel is given by

$$1.51 \times 10^8 \frac{1}{\rho^2} + 1.05 \times 10^5 \alpha \left(\frac{\rho}{\rho_0}\right)^{\frac{2}{3}} M_{\rm f} \ [\rm J]. \tag{2.113}$$

While the energy released by the fusion reaction is

$$M_{\rm f} Q_{\rm DT} f_{\rm b} = 3.4 \times 10^{11} M_{\rm f} f_{\rm b} \ [\rm J] \tag{2.114}$$

and the core gain is estimated as

$$G_{\rm f} = \frac{3.4 \times 10^6 M_{\rm f}}{1.51 \times 10^3/\rho^2 + 1.05\alpha(\rho/\rho_0)^{2/3} M_{\rm f}} \frac{\rho(R_{\rm f} - R_{\rm s})}{\tilde{\beta}(T) + \rho(R_{\rm f} - R_{\rm s})} \tag{2.115}$$

if assuming the achievement of the same level burn fraction $f_{\rm b}$ as the central ignition. Considering 1000-fold compression to the solid density and assuming $R_{\rm s} = 0.002$ cm and $R_{\rm f} = 0.01$ cm, then $M_{\rm f} = 8.8 \times 10^{-4}$ g. Since $\tilde{\beta}(T) = 12.9$ g/cm^2, $G_{\rm f} = 1704$ is achieved.

Next we estimate the output of the ultra intense laser for the fast ignition. By using the above hot spot radius $R_{\rm s} = 0.002$ cm, the required energy for fast ignition is $\mathcal{E}_{\rm h} = 3.4$ kJ with considering $M_{\rm s} = 7.0 \times 10^{-6}$ g. If assuming the efficiency of ultra intense laser to be 30 %, the required laser energy is the order of 10 kJ. To create a dense hot spot, this energy must be injected before the pressure relaxation takes place. The thermal relaxation time between electrons and ions is the order of 10 ps then laser power of 10^{15}W= 1 PW is needed. If $R_{\rm s} = 0.01$ mm, the required beam intensity is 10^{20}W/cm^2.

The pondermotive force $\boldsymbol{F}_p$ by the laser with the frequency ω is given by

$$\boldsymbol{F}_p = -\frac{\omega_p^2}{\omega^2} \nabla \frac{\varepsilon_0 \langle \boldsymbol{E}^2 \rangle}{2} \tag{2.116}$$

where ω_p, $\boldsymbol{E}$ are the plasma frequency of the corona plasma and electric field strength of the laser, respectively. Since the intensity of laser beam peaks at its center, the plasma irradiate by the laser beam with finite radius receives the force by which the plasma is pushed outside of the beam. Thus the density of the plasma is decreased below the cut-off density and the laser beam advances further. Then the dielectric constant of the plasma in the beam $\varepsilon \simeq 1 - \omega_p^2/\omega^2$ becomes larger and works as a convex lens and focus the laser beam (self-focusing). With the repetition of this process laser beam pushes the critical surface and penetrates the laser channel to the dense core region.

The pressure of the fuel compressed to 1000 fold of solid density is 3×10^{15} Pa and the laser light pressure with the intensity of 10^{24} W/m^2 is $I_L/c \sim 3 \times 10^{15}$ Pa, then it is possible to push the critical surface to the dense core by the laser with this level intensity. Once the channel is produced, the energy of laser light can produce fast electrons through $\boldsymbol{J} \times \boldsymbol{B}$ heating due to the effect of oscillating term

in pondermotive force [18] or not-so-resonant resonant absorption (occurs at the frequency coincides half-integral multiples of the plasma frequency) [19], resulting the generation of a hot spot.

This novel idea of fast ignition hadn't put into practice for a long time due to the absence of such a ultra intense laser. However, recently developed chirped pulse amplification (CPA) method [20] enables the production of ultra intense laser pulse (10^{20-21} W/m^2) and illuminated the fast ignition scheme [21]. Moreover, Osaka University developed the remarkable method of using a corn guide [22] and demonstrate high coupling efficiency (20–30 %) of the heating pulse to the hot spot energy through the experiments [23]. These achievements made the fast ignition scheme to be a feasible option.

Chapter 3

Review of Laser Fusion Reactor Design Concept FALCON-D

3.1 Basic ideas of FALCON-D

FALCON-D (Fast ignition Advanced Laser reactor CONcept with a Dry wall chamber) is the design concept of the fast ignition laser fusion reactor with a dry wall chamber and a high repetition laser. Basic idea of FALCON-D is to take the full advantage of the fast ignition scheme and enable a compact dry wall chamber. A dry wall chamber enables high laser repetition and can compensate the reduction of one pulse fusion output. And the compact dry wall chamber and the relatively small number of the laser beams enable a simple maintenance option; cask maintenance method. The following sections review the design point search by 0-D physics model and the design and maintenance method of blanket and the final optics system of FALCON-D.

3.2 Design point search for FALCON-D

3.2.1 Review of the developed simple 0-D analysis model

Basic design point of FALCON-D was selected from the analysis result by using a simple zero-dimensional model. This section gives a brief description of the developed analysis model.

Since we aim the design of laser fusion reactor with a compact dry wall chamber, target yield (fusion energy output per one pulse) need to be reduced as much as possible. However fusion gain of at least 100 is required for a commercial plant to suppress the recirculating power fraction. Then it is necessary to find the minimum target yield with keeping the gain of 100. To estimate the design window, it is useful to examine the relation between the fusion gain and the input energy, called as a "gain-curve". Both the required input energy and the output fusion energy are the function of the parameters which describe the state of the imploded pellet (radius, density and temperature). The required input energy

also depends on several physical processes (e.g., laser-plasma interaction, etc.). As described in chapter 2, these processes are parameterized as the coupling efficiency and the isentrope factor. It is useful to treat these parameters as an input because the contribution of these physics and engineering factors on the plant performance is clarified. Note that several parameters are related each other. The radius of compressed fuel $R_{\rm f}$ relates with the density of the cold fuel region $R_{\rm c}$ and the total mass of the fuel $M_{\rm f}$. In case of central ignition, it also relates with the parameters of hot spot through the pressure equilibrium condition. And the density, radius and temperature of the hot spot are related each other through the self-heating condition.

Then in this model the following five parameters are given as input:

- isentrope factor α
- coupling efficiency of implosion $\eta_{\rm c}$
- coupling efficiency of heating $\eta_{\rm h}$
- fuel compression ratio $\rho_{\rm c}/\rho_0$
- hot spot temperature $T_{\rm s}$
- total mass of the fuel $M_{\rm f}$.

By using the above five parameters, fusion gain G is estimated as the following. As given in the previous chapter, fusion gain G can be written as

$$G = \frac{E_{\rm fus}}{E_{\rm in}} \ , \tag{3.1}$$

where fusion power $E_{\rm fus}$ is given by

$$E_{\rm fus} = Q_{\rm DT} M_{\rm f} f_{\rm b} = Q_{\rm DT} \rho_{\rm f} V_{\rm f} f_{\rm b} \ . \tag{3.2}$$

Here burn fraction $f_{\rm b}$ of Eq. (2.11) is used and parameter β is assumed to have its minimum value, as

$$f_{\rm b} = \frac{\rho_{\rm f} R_{\rm f}}{\rho_{\rm f} R_{\rm f} + \beta_{\rm min}} \ . \tag{3.3}$$

In case of central ignition, the required input energy is given by

$$E_{\rm in}^{\rm central} = E_{\rm f}/\eta_{\rm c} \tag{3.4}$$

where

$$E_{\rm f} = \frac{3}{5} \alpha \varepsilon_F n_{\rm c} V_{\rm f} \tag{3.5}$$

is the internal energy of a compressed fuel. In case of fast ignition, the required input energy is the sum of implosion laser energy and heating laser energy. Considering coupling efficiency of each energy driver, it is given as

$$E_{\rm in}^{\rm fast} = \frac{E_{\rm c}}{\eta_{\rm c}} + \frac{E_{\rm h}}{\eta_{\rm h}} \ . \tag{3.6}$$

where

$$E_{\rm c} = \frac{3}{5}\alpha\varepsilon_{\rm F} n_{\rm f} V_{\rm f} \tag{3.7}$$

and

$$E_{\rm h} = 3 n_{\rm s} k_{\rm B} T_{\rm s} V_{\rm s} \ . \tag{3.8}$$

are the internal energy of a compressed fuel and a hot spot, respectively.

Here in this model the shapes of compressed fuel and hot spot are assumed to be a sphere with radii of $R_{\rm f}$ and $R_{\rm s}$, respectively. Then $V_{\rm f} = (4/3)\pi R_{\rm f}^3$, $V_{\rm s} = (4/3)\pi R_{\rm s}^3$. In case of central ignition, isobaric state is assumed and the density of hot spot is calculated from the density of cold fuel $\rho_{\rm c}$ and hot spot temperature $T_{\rm s}$ through pressure equilibrium condition as

$$\rho_{\rm s} = \frac{\alpha\varepsilon_F \rho_{\rm c}}{5kT_{\rm s}} \ . \tag{3.9}$$

For fast ignition, isochoric state is assumed; $\rho_{\rm s} = \rho_{\rm c} = \rho_{\rm f}$. In both cases, the radius of compressed fuel $R_{\rm f}$ is obtained from the density $\rho_{\rm c}$ and initial fuel mass $M_{\rm f}$. The radius of hot spot $R_{\rm s}$ is calculated to the hot spot temperature $T_{\rm s}$ and density $\rho_{\rm s}$ through the self-heating condition, Eq. (2.22). In case of central ignition, energy loss by mechanical work is regarded as zero ($Q_{\rm m} = 0$), To calculate the D-T fusion reactivity $\langle\sigma v\rangle$, the following approximate formula [24] is used:

$$\langle\sigma v\rangle[{\rm cm}^3/{\rm s}] = C_1\theta\sqrt{\frac{\xi}{m_r c^2 T}}e^{-3\xi} \tag{3.10}$$

where

$$\theta = \frac{T}{1 - \dfrac{T\{C_2 + T(C_4 + C_6 T)\}}{1 + T\{C_3 + T(C_5 + C_7 T)\}}} \tag{3.11}$$

$$\xi = \left(\frac{B_G^2}{4\theta}\right)^{\frac{1}{3}} \tag{3.12}$$

and the constants are

$$B_G = 32.3827,$$

$$m_r c^2 = 1124656,$$

$$C_1 = 1.17302 \times 10^{-9},$$

$$C_2 = 1.51361 \times 10^{-2},$$

$$C_3 = 7.51886 \times 10^{-2},$$

$$C_4 = 4.60643 \times 10^{-3},$$

$$C_5 = 1.35000 \times 10^{-2},$$

$$C_6 = -1.06750 \times 10^{-4},$$

$$C_7 = 1.36600 \times 10^{-5}.$$

However, in the case of fast ignition, the hot spot radius determined by a self heating condition can be much smaller than the focusing limit of heating laser when the hot spot density is high. Then in this model minimum radius of hot spot is set to be 15 μm in reference to the design study of KOYO-Fast reactor.

Consequently we can estimate both the input energy and fusion energy, resulting in the evaluation of the fusion gain.

3.2.2 Design point search

First we carried out the parameter scan to clarify the sensitivity of gain curve on the given parameters. Figures 3.1–3.5 show the dependence of gain curve on the given parameters. Here we select $\rho_f/\rho_0 = 1400$, $T_s = 20$ keV, $\alpha = 2$, $\eta_c = 0.05$ and $\eta_h = 0.2$ as a basic parameter set. These values have been obtained in past experiments and also are assumed in KOYO and KOYO-Fast reactor design study. In each figure parameters which are not scanned are fixed to be these basic values. First one can see fusion gain

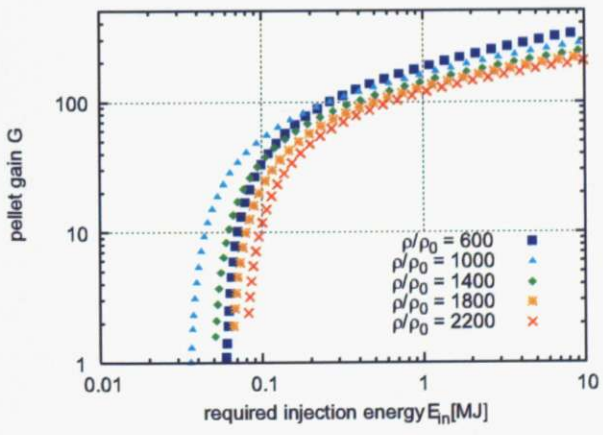

Fig. 3.1: Relation between fusion gain G and input energy $E_{\rm in}$ with various compression ratio $\rho_{\rm f}/\rho_0$.

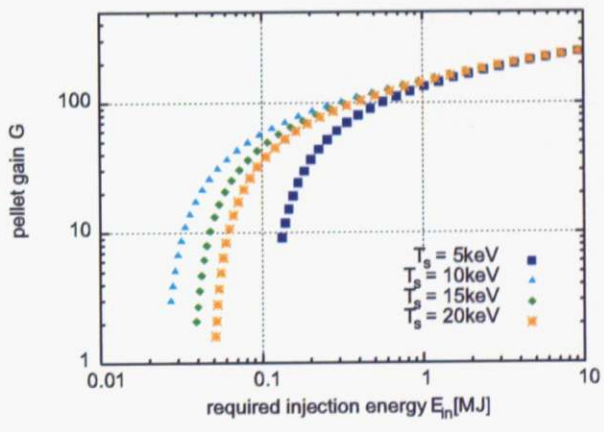

Fig. 3.2: Relation between fusion gain G and input energy $E_{\rm in}$ with various hot spot temperature $T_{\rm s}$.

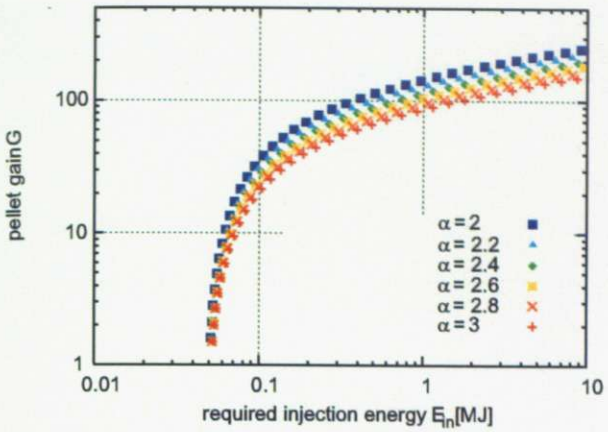

Fig. 3.3: Relation between fusion gain G and input energy $E_{\rm in}$ with various isentrope factor α.

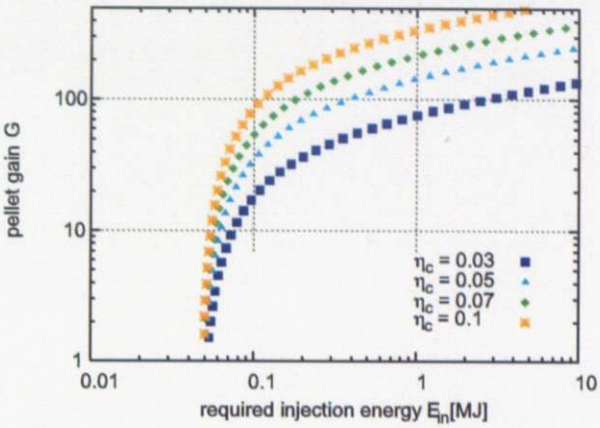

Fig. 3.4: Relation between fusion gain G and input energy $E_{\rm in}$ with various coupling efficiency of implosion laser $\eta_{\rm c}$.

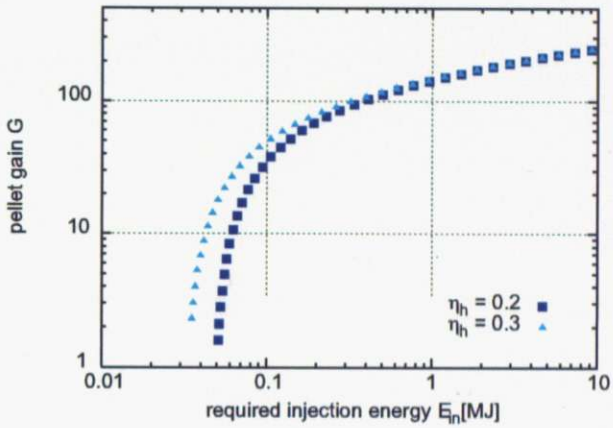

Fig. 3.5: Relation between fusion gain G and input energy $E_{\rm in}$ with various coupling efficiency of heating laser $\eta_{\rm h}$.

increases with decreasing compression ratio especially in high gain ($G > 100$) region. That is because low compression ratio requires low laser energy for implosion. Such low compression ratio also leads to the low density and large radius of the hot spot, resulting in the increase of the energy required for the fast heating. Nevertheless fusion gain still increases because the ratio of the heating laser energy to the total injection energy is quite small. However, the laser for fast heating has ultra high intensity and its energy is limited due to the engineering requirement of the laser glass. Then compression ratio over the range of 1000-1400 is favorable.

One can also see fusion gain has its maximum when the hot spot temperature is around 10 keV. This analysis model is based on the self-heating condition, not the ignition condition, to determine the size of hot spot. Then the heating of a hot spot to temperature higher than 10 keV requires much heating

energy because both the required hot spot radius and temperature increase. However, in high gain region the difference is very little. And actually high temperature hot spot can ignite with lower energy calculated from self-heating condition. Thus there is no concern if the hot spot temperature exceeds 10 keV.

Similarly, coupling efficiency of the heating laser gives little effect on the fusion gain. Then the key parameters that affect much on the gain are isentrope factor and the coupling efficiency of the implosion laser. One can see if $\alpha \geq 3$, there are no solution to achieve $G = 100$ with input energy less than 1 MJ. The coupling efficiency of implosion laser has further great effect on the fusion gain. We can also see the importance of effective implosion from these results.

Then we carried out further analysis for these two parameters. Figure 3.6 shows the gain curve for various isentrope factor and coupling efficiency of implosion. Here compression ratio is assumed to be 1400 (coincides to the density of 300 g/cm^3), and and coupling efficiency of heating laser and heating temperature are assumed to be 0.2, and 20 keV, respectively, based on the design study of KOYO-Fast. For this condition, heating energy is automatically determined to be 50 kJ regardless of other parameters.

It can be seen that fusion gain of 100 is achieved with the input energy of 400 kJ (350 kJ for implosion) with relatively conservative implosion parameters; $\alpha = 2$, $\eta_c = 0.05$. If higher coupling efficiency of implosion $\eta_c = 0.07$ is obtained, the similar design can be achieved with higher isentrope parameter $\alpha = 2.5$. If high coupling efficiency and low isentrope are achieved simultaneously, fusion gain of $G = 135$ can be achieved with $E_{\rm in} = 300$ kJ. Figure 3.7 is the plot of fusion gain as a function of fusion energy output $E_{\rm fus}$. In this figure, gain dependence of central ignition scheme and the design point of KOYO, HAPL (both are central ignition) and KOYO-Fast (fast ignition) are also plotted. One can clearly see the merit of fast ignition, high gain achievement with low fusion energy output, from this figure. According to these results, the minimum target yield that can keep sufficient gain is estimated to be 40 MJ.

Next we consider the possible size of a reactor chamber. From the viewpoint of a construction cost, chamber radius is required to be reduced as much as possible. Then the limit of the heat load on a dry wall is a quite important factor. As described in chapter 5, tungsten is a candidate of the material that exposed to high heat load because it has the highest melting point (3680 K) and good thermal properties (e.g., high thermal conductivity) in high temperature region. The specific heat of tungsten is 0.15 J/g/K $\sim$ 3 J/cm^3/K. Then assuming the thickness of heat deposition depth is 5 μm and uniform heating of the region, heat flux for 1 K temperature increase of the region is 1.5×10^{-3} J/cm^2. Thus

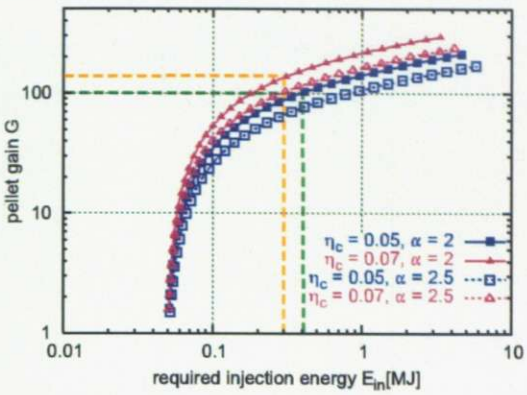

Fig. 3.6: Relation between fusion gain G and input energy $E_{\rm in}$ with various implosion parameters.

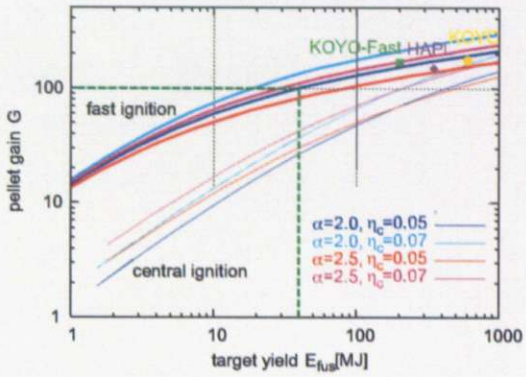

Fig. 3.7: Relation between fusion gain G and fusion energy output $E_{\rm fus}$ with various coupling efficiency of implosion laser $\eta_{\rm c}$. The relation in case of central ignition and the design points of other studies are also plotted.

within the heat flux of 4–5 J/cm^2, the increase of temperature of the region is confined below 3000 K. If assuming ferritic steel for the structural material, base temperature is limited up to 700 K to avoid erosion. Then heat flux of 4–5 J/cm^2 does not cause surface melting of tungsten. Here we considered some safety margin and selected 2 J/cm^2 for the limit of the heat flux. Then possible minimum chamber radius is 5.64 m. Considering major radii of most of conceptual designs of a commercial tokamak reactor is around 5–6m, this size chamber can be a possible candidate for a commercial plant when considering its construction cost.

However, it must be examined that:

- the possibility of achievement of sufficient fusion gain ($G \geq 100$) with such small input energy ($E_{\rm c} = 350$ kJ and $E_{\rm h} = 50$ kJ),
- dry wall survival under harsh condition of IFE during long period commercial operation.

Then one-dimensional hydrodynamic simulation of core plasma dynamics and thermomechanical analysis of the dry first wall were carried out. The detailed studies about them are given in the following chapters.

3.3 Maintenance method of FALCON-D

One of the remarkable features of FALCON-D is its simple maintenance method that utilizes the compact dry wall chamber. A fusion power plant needs to replace its first wall and blanket structural material because they are damaged by the fast neutron irradiation. As shown in chapter 5, the first wall of an IFE reactor also irradiated by high energy X-rays and charged particles, which leads to higher damage of the first wall. In case that solid breeder is used, the whole blanket systems need to

be replaced because of the decrease in tritium breeding ratio (TBR) due to the reduction of lithium amount. In addition, a laser fusion reactor must periodically replace its final optical components because they directly see the chamber center and the damage due to neutron irradiation is inevitable.

The next section gives a brief review of the blanket system of FALCON-D. In the succeeding subsections, maintenance scheme of blanket system and final optics are discussed.

3.3.1 Blanket and heat transport system

Since FALCON-D is assumed to be in a commercial use, it must has the blanket system that can achieve sufficient TBR. At present, the following 7 types of blanket system have been proposed for the test blanket module (TBM) for the ITER [25].

1. WCSB/WCCB/WCPB (Water-Cooled Solid Breeder/Ceramic Breeder/Pebble Beds)
2. HCSB/HCCB/HCPB (Helium-Cooled SB/CB/PB)
3. HCLL (Helium-Cooled Lithium Lead)
4. DCLL (Dual-Coolant Lithium Lead)
5. DCMS (Dual-Coolant Molten Salt)
6. SCL (Self-Cooled Liquid Lithium)
7. HCLi (Helium-Cooled Liquid Lithium)

Since there are no magnetic fields in blanket region in an IFE reactor, a liquid breeder blanket is free from MHD pressure loss, one of the most critical problems on using a liquid breeder in a magnetic fusion plant. Liquid breeders have higher TBR than solid ones and do not need beryllium neutron multiplier, of which high chemical toxicity and chemical activity is highly concerned. Then liquid breeders are favorable for the blanket for an IFE reactor. Such liquid breeders, however, must operate in high temperature above the melting point and then some advance materials (silicon carbide, vanadium alloy, etc.) are required for the structural material to satisfy compatibility with the breeder. And they also cannot use water coolant, which is widely used in the present commercial plants and has a high technological reliability. Thus Japan has insisted that WCSB blanket should be installed in ITER TBM to ensure the feasibility of the blanket system. In the conceptual design of a commercial reactor, it is also important to consider the possibility of the use of WCSB blanket. Actually some conceptual designs of Tokamak commercial reactor, for example, CREST (Compact REversed Shear Tokamak) [4] designed by CRIEPI, also consider the use of WCSB blanket.

Thus here we also selected the WCSB blanket. For the breeder, we select lithium titanate (Li_2TiO_3) because of its relatively low chemical reactivity. We choose pair of reduced activated ferritic steel (F82H) and water for the structural material and coolant of the blanket, that has high technological feasibility and reliability.

The blanket design refers to that of CREST. In the design of CREST, the relatively high plant thermal efficiency, $\eta_{th} \sim 0.4$, is achieved by utilizing overheated steam cycle. In this design, the inlet temperature of coolant required to below 673 K to suppress the temperature increase of the first wall surface (see details in chapter 5). However, high outlet coolant temperature is simultaneously required to achieve high plant thermal efficiency, Then here we assumed supercritical water as a coolant and expected to achieve both low coolant temperature (623 K) in the first wall and high outlet temperature (773 K) by adjusting the path of the coolant channel (see Fig. 3.8). Then thermal efficiency of $\eta_{th} = 0.4$ is expected in FALCON-D.

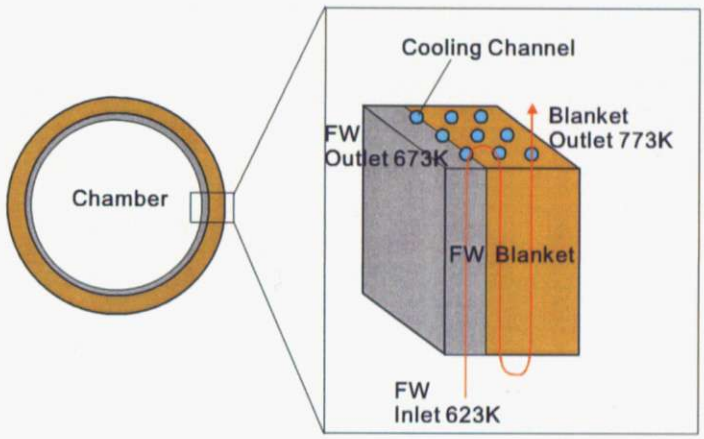

Fig. 3.8: Schematic viewing of the coolant channel

The major issue in lithium titanate breeder is its low TBR. However, in FALCON-D, high blanket covering ratio (> 0.9) is expected and the total TBR is estimated to be 1.22 according to the calculation with MCNP (Monte Carlo N-Particle) code [26]. This value is sufficient one for a commercial operation. This high blanket coverage can be said to be one of the merits of an IFE reactor.

3.3.2 Maintenance method of blanket system

After the operation for the certain time (expected to be about one year in accordance to nuclear fission plant), the first wall and the blanket material are activated by the fast neutron radiation. They also contain specific amount of tritium. Thus the replacement of them must be held in closed environment.

Generally, there are two methods for the blanket replacement approach. One is in-situ method, that uses a remote manipulator arm with a maintenance rail. ITER adopts this method. The other is cask method, that uses a large cask with a large maintenance port for the replacement. From the viewpoint of the plant availability, the latter method is favorable because it effectively reduces the time to unfasten, fasten and check the joints of the structure component and the heat transfer system. Hence, the latter method was selected in several commercial tokamak power plant concepts [28, 29].

FALCON-D also adopts the cask method to reduce the maintenance time. In tokamak reactor, blanket and surrounding components are divided into several sectors and withdrawn to the horizontal direction into the cask connected the side wall of the vacuum chamber. But in an IFE reactor, multiple beam lines surround the vacuum vessel and it is difficult to withdraw components to the horizontal direction. The total mass of blanket of FALCON-D is relatively small because of its small chamber radius. Then we considered to extract and install the blanket system through the upper port.

In a laser fusion reactor, beam line directly sees the chamber center and it is impossible for the vacuum vessel to have the function of neutron shield. Thus it is considered that almost all reactor core components except the final optical device of the heating beam are placed in the reactor room, that is, the wall of the reactor room serves as a role of neutron shield. Then blanket system can be separated from the vacuum vessel. This separation leads to the following merits for the maintenance:

- blanket need not to work as a vacuum boundary and it can be easily divided into several sectors.
- separation and joint of multiple ducts or pipes can be held in wide vacuum space between vacuum vessel and blanket.
- only the first wall and blanket components need to be extracted and the size of cask and the force of crane are reduced.
- beam ducts for all beam lines need to be set up only outside the vacuum vessel and better accessibility of a large cask is achieved.

The elevation view of FALCON-D reactor building is shown in Fig. 3.9

The larger number of sectors, the less weight of one sector. But maintenance time increases with the number of sectors. In FALCON-D the number of beam lines for implosion laser is assumed to be 32 in reference to the design of KOYO-Fast reactor. To achieve spherical symmetry, those beam lines correspond to the lines between the center and the vertex or the center of gravity in each surface of the regular icosahedrons (20-polyhedron). In this case there are two beam injections from both poles to the reactor core and the upper pole beam line is an obstacle to the maintenance. It is considered that more

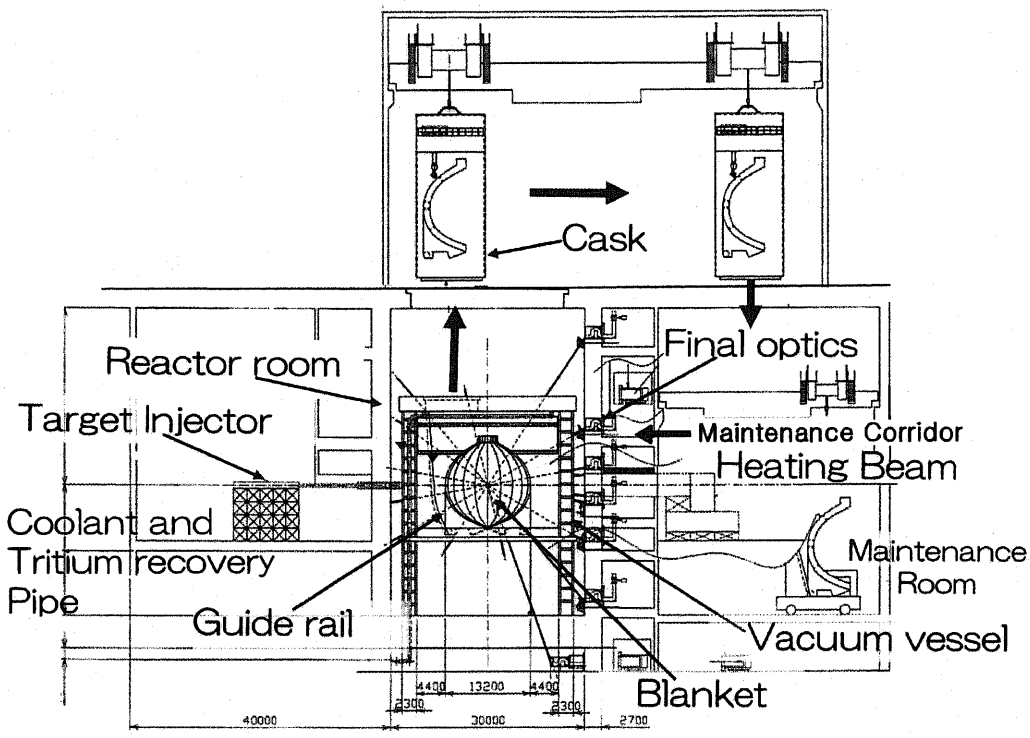

Fig. 3.9: Elevation view of the FALCON-D reactor building

than 30 laser beam lines are needed to achieve the good uniformity during the compression of the fuel pellet [27]. However, the fast ignition scheme does not require so much good laser uniformity compared with the central ignition scheme. Thus we considered that the removal of the upper pole beam line is possible. Then the blanket is divided into 20 sectors so that all of 32 beam lines (1 beam for heating laser) cross the edge between blanket sectors. Then the weight of each blanket sector is estimated to be 100 tons, based on the blanket design of the tokamak reactor concept Demo-CREST [28].

The detailed replacement procedure of blanket system is the following. The each sector of the blanket system is extracted and installed through the upper large port. Correspondingly, 20 maintenance ports exist on the ceiling of the vacuum vessel. The cask accesses to those maintenance ports. After the cask door is attached to the port door, the door of the maintenance port is opened together with the cask door to the inside of the cask. Figure 3.10 shows the cask attached to the maintenance door of the vacuum vessel. Then each blanket sector is extracted by a crane after the cut of the connections of the heat transfer and tritium recovery system shown in Fig. 3.9 by a remote handling device. To avoid the shaking of the sector during extraction, the guide rails are located corresponding to each blanket sector.

Then cask is moved to the maintenance room, that locates adjacent to the reactor room. The replaced blanket system is transported and installed through the inverse process of the extraction. Each blanket sector has a joint on its bottom side to stand by itself.

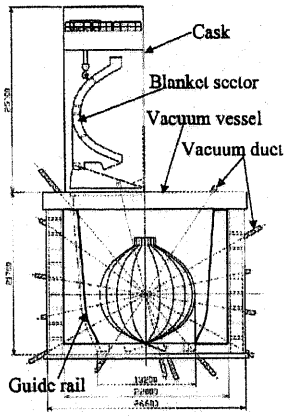

Fig. 3.10: Schematic drawing of the blanket replacement with the guide rail and the cask

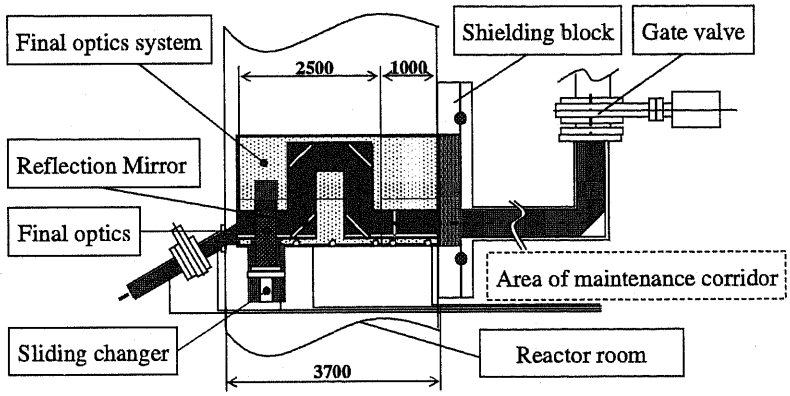

Fig. 3.11: Schematic viewing of final optics system of FALCON-D with sliding changer

3.3.3 Design and maintenance option of the final optics system

Figure 3.11 shows the schematic view of the final optics system of the implosion laser. The U-shape duct in the system can reduce the total neutron flux at outside of the reactor room to the order of 10^8 $n/cm^2/s$ [26], which is one order lower than that at just outside the shield blanket in a tokamak reactor concept CREST. This final optics system is placed in the wall of the reactor room, as shown in Fig. 3.9. The locations of final optics system are divided into 7 groups with a different level corresponding to the polar angle of the beam lines. To access the final optics system, 7 access corridors are placed at the corresponding level. At all levels the corridor surrounds the reactor room and a remote handling device can access the all final optics systems located on the same level. The radiation damage of the final optics strongly affects the maintenance frequency. According to the design criterion of the diagnostics window (quarts) for the ITER [30], the limit of the total fast neutron fluence above 100 keV is assumed to be $3.0 \times 10^{20} n/cm^2$. Assuming this value as the upper limit, the final optics system must be replaced, at least, every half year. Then we proposed "sliding changer" (SC) system for the final optics (prism) of the implosion laser. Two prisms are prepared on this SC and it can replace the prism by just sliding in vertical direction. Thus the replacement frequency of the whole final optics system can be reduced to once per a year.

Figure 3.12 shows the maintenance procedure of the final optics system. First two gate valves

located on the both side of the final optics system are closed and the gas in the beam duct, which contains tritium, is removed. Then the shielding block at the outer side of the system is shut and the laser guidance duct is separated and removed. After that, a cask-type replacement device with a shielding block is jointed. Then two shielding block are opened and final optics system is extracted into the cask. Finally two shielding blocks are shut again and the replacement device is transported to the maintenance room by the transportation chassis.

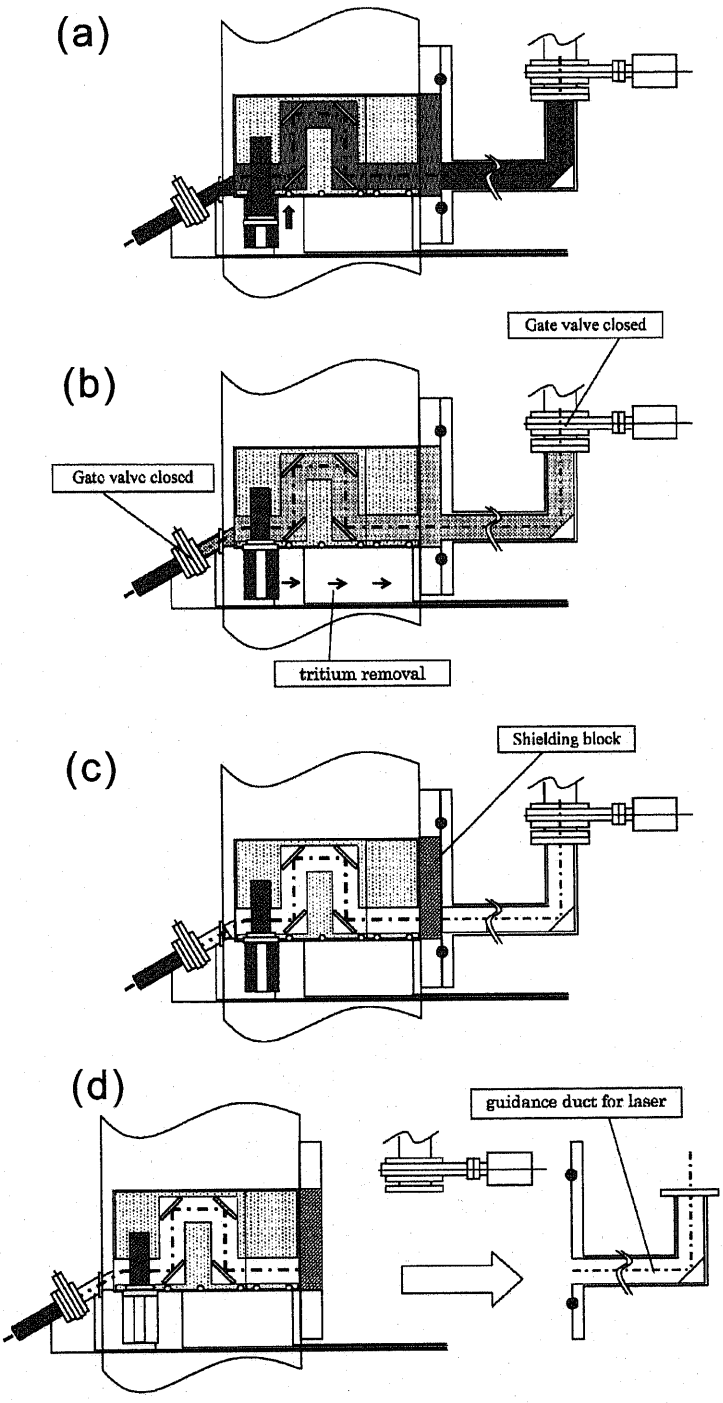
(a)
(b)
Gate valve closed
Gate valve closed
tritium removal
(c)
Shielding block
(d)
guidance duct for laser

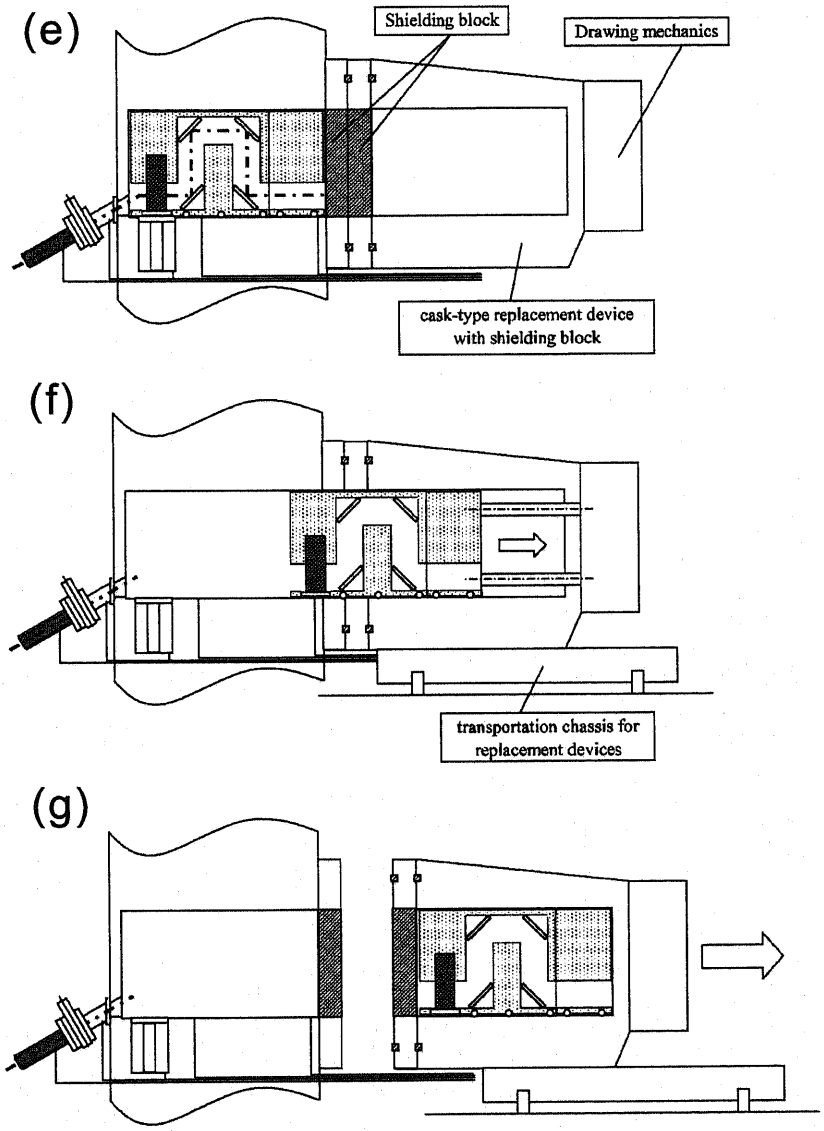

Fig. 3.12: Replacement method of the final optics system. (a)The sliding changer is elevated to the upper level. (b)Two gate valves are closed and the gas containing tritium is removed. (c)The shielding block is shut. (d)The guidance duct is separated and removed. (e)A cask type replacement device is jointed. (f)Two shielding blocks are opened and the final optics system is extracted into the cask. (g)The shielding blocks are shut and the replacement device is transported by the transportation chassis.

Chapter 4

Core Plasma Analysis by Hydrodynamic Code ILESTA 1-D

4.1 Objective

To achieve a compact dry wall chamber, target yield must be minimized with keeping the sufficient fusion gain. The estimation by 0-D analysis model given in previous chapter shows the possibility of achievement of fusion gain $G = 100$ with laser energy of 400 kJ (350 kJ for implosion, 50 kJ for heating). This result, however, is based on three assuming parameters; $\alpha = 2.0$, $\eta_c = 0.05$ and $\rho/\rho_0 = 1400$. These parameters have already been demonstrated in several experiments. They were also assumed in the commercial plant design, KOYO-Fast. But this design study is probably the first case that considers the design point with such marginal fusion gain for a commercial plant design. Thus feasibility of such low yield, high gain design must be examined by the further detailed analysis. In addition, as described in the following, fast ignition scheme can greatly relax the physics requirements on the pellet implosion compared with the conventional central ignition scheme. This property enables higher flexibility on core plasma design; the pellet design and laser pulse shaping. It is important to carry out optimization study of core plasma from the viewpoint of the utilization of the fast ignition. Core plasma is also a source of X-rays and charged particles that cause high heat load on a dry wall as well as an energy multiplier in the plant system. Then it is important to obtain the detailed data of such threatening spectra for the discussion of the design feasibility of a dry wall, given in the next chapter.

To satisfy the above three requirements, we have introduced one-dimensional hydrodynamic simulation code ILESTA-1D and performed simulation of pellet implosion and burning. In the following, a brief description of ILESTA-1D code and the result of The optimization study of core plasma are given.

4.2 Hydrodynamic simulation code ILESTA-1D

4.2.1 Set of equations

ILESTA-1D is a one-dimensional hydrodynamic simulation code developed by ILE (Institute of Laser Engineering), Osaka University. The one-fluid, two-temperature fluid model is used in the code. This code includes following seven equations and can simulate all physics involved in an implosion and burning of the laser fusion fuel pellet.

$$\frac{\mathrm{d}\rho}{\mathrm{d}t} = -\rho\nabla\cdot\boldsymbol{u} \tag{4.1}$$

$$\rho\frac{\mathrm{d}\boldsymbol{u}}{\mathrm{d}t} = -\nabla P \tag{4.2}$$

$$\rho\frac{\mathrm{d}\varepsilon_i}{\mathrm{d}t} = -P_i\nabla\cdot\boldsymbol{u} - \nabla\cdot\boldsymbol{q}_i + Q_{ei} + S^i_\alpha \tag{4.3}$$

$$\rho\frac{\mathrm{d}\varepsilon_e}{\mathrm{d}t} = -P_e\nabla\cdot\boldsymbol{u} - \nabla\cdot\boldsymbol{q}_e - Q_{ei} + S_\mathrm{L} + S_\mathrm{r} + S^e_\alpha \tag{4.4}$$

$$\frac{1}{c}\frac{\partial I^\nu}{\partial t} + \boldsymbol{n}\cdot\nabla I^\nu = \eta^\nu - \chi^\nu I^\nu \tag{4.5}$$

$$\frac{\partial\phi^\alpha}{\partial t} + \boldsymbol{v}\cdot\nabla\phi^\alpha = S_\mathrm{DT} + \left(\frac{\partial\phi^\alpha}{\partial t}\right)_\mathrm{coll} \tag{4.6}$$

$$\boldsymbol{v}_g\cdot\nabla I^k_\mathrm{L} = -\nu_\mathrm{abs} I^k_\mathrm{L} \tag{4.7}$$

In equation of continuity Eq. (4.1), ρ is the mass density and $\boldsymbol{u}$ is the flow velocity. Since the electron density is negligible compared to the ion density, density is defined as $\rho = m_i n_i$, where m_i, n_i are the average mass of an ion and the number density of ions, respectively. In Eq. (4.2), P is the total pressure;

$$P = P_e(\rho, T_e) + P_i(\rho, T_i) \tag{4.8}$$

where P_e and P_i are the electron and ion pressures, and T_e and T_i are electron and ion temperatures, respectively. Since temperature and density of the plasma of inertial fusion vary very wide range ($10^{-3} \lesssim T \lesssim 10^5$ eV, $0.1 \lesssim \rho \lesssim 10^3$ g/cm^3), these pressures cannot be obtained from equation of state of ideal gas only. Then ILESTA uses quotidian equation of state (QEOS) [31] to calculate the pressure from the temperature and density. QEOS is a self-contained theoretical model that requires no external data base and supplies the complete set of thermodynamic properties including entropy. A brief description of the model of equation of state used in ILESTA code is given in the reference [32].

Equation (4.3) is the equation of ion internal energy. Here ε_i is the ion internal energy per unit mass and is the function of its density and temperature $\varepsilon_i = \varepsilon_i(\rho, T_i)$. The first term in the right-hand side in Eq. (4.3) is the pressure work term. The second term $\nabla\cdot\boldsymbol{q}_i$ is energy transported by ion thermal conduction. Here $\boldsymbol{q}_i$ is the ion heat fluid and calculated by the following diffusion type expression;

$$\boldsymbol{q}_i = -\kappa_i\nabla T_i \equiv -\frac{\ell_i v_i}{3}\nabla T_i \tag{4.9}$$

where ℓ_i, v_i, κ_i are the ion mean-free-path, thermal velocity and thermal conductivity, respectively. The third term Q_{ei} is the ion-electron energy relaxation term. The last term S_α^i is the energy source through the alpha-particle heating.

Eq. (4.4) is the equation of the electron internal energy. Here ε_e is the electron internal energy per unit mass, which is consists of the contributions from free electrons and bound electrons. In the right-hand side of Eq. (4.4), $\nabla \cdot \boldsymbol{q}_e$ is the energy transported by the electron thermal conduction. Similar to the case of ions, the electron heat flux is described by the diffusion type model;

$$\boldsymbol{q}_e = -\kappa_e \nabla T_e \equiv -\frac{\ell_e v_e}{3} \nabla T_e \tag{4.10}$$

where ℓ_e, v_e, κ_e are the electron mean-free-path, thermal velocity and thermal conductivity, respectively.

Equation (4.5) is the equation of radiation transport. Here superscript ν indicates the value is related to the spectral range from ν to $\nu + \mathrm{d}\nu$. In this equation, I^ν is the spectral radiation intensity, c is the speed of light, and $\boldsymbol{vn}$ is the unit vector parallel to the direction of radiation propagation. In the right-hand side of Eq.(4.5), η^ν is the spontaneous emission rate (emissivity) per unit volume, unit time, unit solid angle. χ^ν is the absorption coefficient (we call "opacity" in what follows) that is consists of pure absorption minus the induced emission contribution. In ILESTA code, this radiation transport is solved by the flux-limited diffusion model. Opacity and emissivity is obtained from tabulated data base, which is generated by collisional radiative equilibrium (CRE) model.

Equation (4.6) is a kinetic equation of alpha particles produced by D-T fusion reaction. In RHS of Eq. (4.6), S_{DT} is a source term and $(\partial \phi^\alpha / \partial t)_{\mathrm{coll}}$ represents slowing down by Coulomb collisions with background ions and electrons. In ILESTA code, Eq. (4.6) is solved by reducing to an equation of the multi-group, flux-limited diffusion model [33]. In the model, alpha particles are divided into $g_{\max}$ groups by an energy mesh, in which the boundaries of the g-th group are at E_g and E_{g+1}. Then (4.6) is reduced to the diffusion equation of the number density of alpha particles in energy group g;

$$\frac{\partial N_g}{\partial t} = \nabla \cdot (D_g \nabla N_g) - \frac{N_g}{\tau_g} + S_g \quad (g = 1, 2, \ldots, g_{\max}) \tag{4.11}$$

where D_g, τ_g and S_g are diffusion coefficient, energy slowing down time to the adjacent lower energy group $g-1$ and source term for energy group g, respectively. Source term except for the highest energy group is the contribution of slowing down of the adjacent higher energy group. For the highest energy group, source term is equal to the S_{DT} in Eq. (4.6). Then note that this model can only describe slowing down of 3.5 MeV D-T alpha particles into lower energy.

Equation (4.7) gives the propagation and absorption of laser light. In this equation, laser photon is assumed to propagates in plasmas with the group velocity $\boldsymbol{v}_g$ and its absorption is described by the

absorption coefficient $\nu_{\rm abs}$. In Eq. (4.7), $I_{\rm L}^k$ is the laser intensity of a given beamlet "k" and it also gives the term $S_{\rm L}$ of Eq. (4.4) through the relation;

$$S_{\rm L} = \sum_k \frac{\nu_{\rm abs} I_{\rm L}^k}{v_g^k} \ . \tag{4.12}$$

To solve Eq. (4.7) the ray-tracing method is used.

4.2.2 Simulation of fast ignition

Since ILESTA-1D is the one-dimensional simulation code, it cannot reproduce the detailed physics of fast ignition, which is essentially asymmetric nature. However, it is worthwhile if we can estimate the effect of fast heating by a 1-D code because its rapid computation enables parameter scan over a wide range about the parameters specified in fast ignition (e.g., the timing of heating, heating energy). Then we tried to simulate the effect of fast heating by ILESTA-1D.

Since the velocity of burn wave is the same order of the α particle velocity (10^7 m/s for 3.5 MeV α) and much larger than the expanding velocity of burning fuel pellet ($\sim 10^5$ m/s), the location of the heating region is considered to give little effect on the final state of burnt fuel.

Actually fast heating is caused by the fast electron generated through the relativistic interaction with an ultra intense laser and a dense core plasma. The detailed mechanism of this laser-plasma interaction has not yet become clear and here we only consider the coupling efficiency from the heating laser to the energy of the fast electrons. These fast electrons deposit the energy on the core plasma mainly through a direct collision with plasma electrons. Then the size of heating region depends on the beam size and the range of fast electron in the core plasma, which strongly depends on the energy spectrum of the fast electrons. In 1-D code the shape of heating region cannot be given because the heating region must be a sphere or spherical shell. And the heating of the region except for the center gives unphysical result of heating of spherical shell region. Thus the heating region is fixed to be the center of the compressed pellet and the radius of heating region is determined so that the areal density (density-radius Product) of heating region is equal to 0.4 g/cm^2. This areal density coincides to the range of 2 MeV electron, which is observed in the experiments with a gold target. As described in the above, the main mechanism of heating is direct collision between fast and bulk electrons in the core plasma. Thus we introduce an artificial heating term in the energy equation of the electrons (Eq. (4.4)) to simulate fast heating. For simplicity the time profile of the heating is constant during the pulse width of the heating laser. The spatial profile of energy deposition is determined by the density of each computational mesh. Figure 4.1 shows the schematic image of this modeling. Since the collision rate between fast and bulk electrons is proportional to the density of bulk electrons, the energy is prorated based on the electron density

of each mesh, which physically corresponds to the uniform heating of the electron. The total heating energy, time duration, and coupling efficiency are externally given.

Figure 4.2 shows the comparison of temporal evolution of electron temperature around the time at maximum compression with and without external heating. As you can see, the electron temperature at the core region increases abruptly to 15 keV immediately after the injection of the external heating energy (at 18.10ns). This leads to ion heating through temperature relaxation between electrons and ions and resulting in ignition and fusion burn. By contrast, electron temperature without external heating is up to 5 keV and no fusion burn occurs. This result indicates the fast heating effect is successfully reproduced in one-dimensional hydrodynamic code.

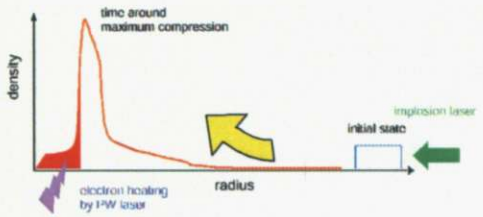

Fig. 4.1: Schematic view of the model for fast heating simulation in 1-D hydrodynamic code. The red curve describes the radial density profile at the timing of maximum compression. The external heating energy is injected in the hatched region.

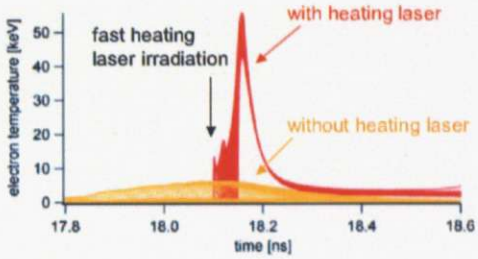

Fig. 4.2: Temporal temperature evolution of electron temperature in 1-D hydrodynamic simulation. Red curves shows the result with external heating which emulates the fast heating.

4.3 Hydrodynamics of spherical pellet implosion

4.3.1 Analytic model of isentropic compression

To achieve an extremely high density compression, one method has been proposed in which the absorbed laser power is controlled with time so that the pellet compression takes place nearly isotropically.

At first, the theoretical and numerical works were carried out to achieve homogeneous isentropic compression of a spherical pellet filled with solid fuel [34]. However, this method becomes impossible when the Mach number of the flow, the ratio of the flow speed to the adiabatic sound speed, anywhere exceeded the value $\sqrt{3}$. Thus the achievable density is limited and peak power to achieve the ρR value required for the sufficient gain cannot be reduced so much. Then to achieve isentropic compression with high Mach number, it has proposed to compress thin hollow shells instead of solid droplets [35]. Here a brief review of the theory of isentropic compression of hollow shells is given.

First we define the velocity field of the form

$$u(r,t) = \frac{r}{R_0(t)}\frac{\mathrm{d}R_0(t)}{\mathrm{d}t} \tag{4.13}$$

where $R_0(t)$ is the trajectory of a given fluid element. In what following R_0 denotes the outer boundary of a spherical gas. By using this velocity, next analytic solutions for radial flow in spherical geometry is discussed.

Consider the radial trajectory $R(a,t)$ of a fluid element with Lagrange coordinate a, the velocity of this elemental is given by

$$u(a,t) = \frac{\partial R(a,t)}{\partial t} \ . \tag{4.14}$$

Substituting this into Eq. (4.13) and setting $r = R(a,t)$, we obtain the relation

$$\frac{1}{R(a,t)}\frac{\partial R(a,t)}{\partial t} = \frac{1}{R_0(t)}\frac{\mathrm{d}R_0(t)}{\mathrm{d}t} \tag{4.15}$$

Integrating Eq. (4.15) over time from 0 to t, yielding

$$\frac{R(a,t)}{R(a,0)} = \frac{R_0(t)}{R_0(0)} \ . \tag{4.16}$$

Here we define the above ratio of radius as $h(t)$ and also define

$$R_0 \equiv R_0(0), \qquad a \equiv \frac{R(a,0)}{R_0}, \tag{4.17}$$

then one finds

$$\frac{R(a,t)}{R_0} = ah(t) \ . \tag{4.18}$$

According to the mass conservation law:

$$\rho(a,0)R(a,0)^2\mathrm{d}R = \rho(a,t)R(a,t)^2\mathrm{d}R \ , \tag{4.19}$$

we finds

$$\rho(a,t) = \frac{R_0^3 a^2 \mathrm{d}a}{R(a,t)^2\mathrm{d}R}\rho(a,0) = \frac{\rho(a,0)}{h(t)^3} \ . \tag{4.20}$$

Here we use the relation $R(a,0)^2\mathrm{d}R = R_0^3 a^2 \mathrm{d}a$. From the adiabatic law with $\gamma = 5/3$, we also obtain the relation

$$p(a,t) = p(a,0)\left[\frac{\rho(a,t)}{\rho(a,0)}\right]^{\frac{5}{3}} = \frac{p(a,0)}{h(t)^5} \ . \tag{4.21}$$

The equation of conservation of momentum for spherical geometry in Lagrange representation is given as

$$\frac{\partial u}{\partial t} = -\frac{R^2}{\rho_0(a)a^2}\frac{\partial p}{\partial a} \ . \tag{4.22}$$

By using the definition of $R(a,t)$ and a in the above, it is rewritten in the form

$$\frac{\partial^2 R(a,t)}{\partial t^2} = -\frac{R(a,t)^2}{\rho_0(a,0)R_0^3 a^2}\frac{\partial p(a,t)}{\partial a} \ . \tag{4.23}$$

Then substituting the relations

$$\frac{\partial^2 R(a,t)}{\partial t^2} = R_0 \frac{\partial^2}{\partial t^2} a h(t) \tag{4.24}$$

$$\frac{\partial p(a,t)}{\partial a} = \frac{\partial}{\partial a}\frac{p(a,0)}{h(t)^5} = \frac{1}{h(t)^5}\frac{\partial p_0(a)}{\partial a} \tag{4.25}$$

$$\frac{R(a,t)^2}{R_0^3 a^2} = \frac{a^2 h(t)^2}{R_0 a^2} = \frac{h(t)^2}{R_0} \tag{4.26}$$

into Eq. (4.22), one finds

$$a R_0 \frac{\partial^2 h(t)}{\partial t^2} = -\frac{1}{\rho_0(a) R_0}\frac{1}{h(t)^3}\frac{\partial p_0(a)}{\partial a} \ . \tag{4.27}$$

Then finally we obtain

$$h(t)^3 \frac{\partial^2 h(t)}{\partial t^2} = -\frac{1}{R_0^2 \rho_0(a) a}\frac{\partial p_0(a)}{\partial a} = \text{const.} \equiv \pm\frac{1}{t_0^2} \ , \tag{4.28}$$

where time and space dependent terms are separated and then it can described by a separation constant. For initial conditions $h = 1$ and $\mathrm{d}h/\mathrm{d}t = 0$ at $t = 0$, corresponding to a fluid initially at rest, the time-dependent part of Eq. (4.28) can be integrated analytically, yielding

$$h(t) = \sqrt{1 \pm \left(\frac{t}{t_0}\right)^2} \ . \tag{4.29}$$

Here minus sign describes imploding flow. It indicates the compression of the enclosed mass to arbitrary density in a perfectly adiabatic manner is possible. On the other hand, the plus sign describes a flow imploding for $t < 0$ and exploding for $t > 0$, and reaching a state of maximum, but finite, compression at $t = 0$. This solution is useful to model the stagnation phase.

4.3.2 Analytic model for cumulative implosion

Here we discuss about the minus-sign solution of Eq. (4.29) in more detail. Let us consider the condition

$$R_0(t) = R_0 h(t), \tag{4.30}$$

which corresponding to $a = 1$. And normalizing density and pressure by the initial values at the surface;

$$\frac{\rho(a,0)}{\rho_0} = G(a), \tag{4.31}$$

$$\frac{p(a,0)}{p_0} = P(a). \tag{4.32}$$

Then the spatial part of Eq. (4.28) becomes

$$\frac{1}{G(a)a}\frac{\mathrm{d}P(a)}{\mathrm{d}a} = \frac{(R_0/t_0)^2}{p_0/\rho_0} \tag{4.33}$$

with boundary conditions $G(1) = P(1) = 1$. Considering a gas of uniform entropy, $p_0/\rho_0^{5/3} = \mathcal{A}_0$ and $P(a) = G(a)^{5/3}$, Eq. (4.33) can be rewritten as

$$\frac{\mathrm{d}G(a)^{\frac{2}{3}}}{\mathrm{d}a} = 2a\frac{(R_0/c_0t_0)^2}{3} \,. \tag{4.34}$$

Here we use the relations

$$\frac{\mathrm{d}P}{\mathrm{d}a} = \frac{\mathrm{d}G^{\frac{5}{3}}}{\mathrm{d}a} = \frac{5}{3}G^{\frac{2}{3}}\frac{\mathrm{d}G}{\mathrm{d}a}, \qquad \frac{\mathrm{d}G^{\frac{2}{3}}}{\mathrm{d}a} = \frac{2}{3}G^{-\frac{1}{3}}\frac{\mathrm{d}G}{\mathrm{d}a} \,. \tag{4.35}$$

and

$$c_0 = \sqrt{\frac{5p_0}{3\rho_0}} \tag{4.36}$$

denotes the adiabatic sound velocity at the surface.

Here considering a hollow shells with an inner surface at some element a_i. The integration of Eq. (4.34) yields

$$G(a) = \left[\frac{(a^2 - a_i^2)(R_0/c_0t_0)^2}{3}\right]^{\frac{3}{2}} \,. \tag{4.37}$$

Considering boundary condition $G(1) = 1$, one finds

$$t_0^2 = \frac{R_0^2(1-a_i^2)}{3c_0^2} \,. \tag{4.38}$$

Then substituting this into Eq. (4.37), we obtain

$$G(a) = \left(\frac{a^2 - a_i^2}{1 - a_i^2}\right)^{\frac{3}{2}} \,. \tag{4.39}$$

Then by using the condition $P(a) = G(a)^{5/3}$, we also find

$$P(a) = \left(\frac{a^2 - a_i^2}{1 - a_i^2}\right)^{\frac{5}{2}} \,. \tag{4.40}$$

Note that these solutions do not describe an initial pellet shell with uniform density and zero pressure. However, they rather useful because these profiles are close to those at the time when the first sequence of shock and rarefaction waves have passed.

For thin shells with a thickness $d = (1 - a_i)R_0 \ll R_0$, the aspect ratio ζ_A can be approximated as

$$\zeta_A = \frac{R_0}{d} = \frac{1}{1-a_i} = \frac{1+a_i}{1-a_i^2} \simeq \frac{2}{1-a_i^2} \,. \tag{4.41}$$

Then we obtain the implosion time of thin shells

$$t_0 \simeq \sqrt{\frac{2}{3}}\frac{R_0}{c_0}\frac{1}{\sqrt{\zeta_A}} \,. \tag{4.42}$$

Taking R_0/c_0 as a constant, it is seen that thin shells implode faster than thick shells. However, hydrodynamic instabilities of the Rayleigh-Taylor type limits the thinness of the fuel. The physics of Rayleigh-Taylor instability in the pellet implosion is reviewed in the next subsection.

We can estimate the mechanical power P_{M} required to achieve the implosion discussed in the above. The mechanical power by the pressure work can be estimated as

$$P_{\mathrm{M}} = PuS = 4\pi R^2 Pu = 4\pi (R_0 h)^2 \frac{p_0}{h^5} R_0 \frac{\mathrm{d}h}{\mathrm{d}t} \ . \tag{4.43}$$

Then substituting Eq.(4.29) into this, one obtains

$$P_{\mathrm{M}}(t) = \frac{4\pi R_0^3 p_0}{t_0} \frac{t/t_0}{\left[1-(t/t_0)^2\right]^2} \ . \tag{4.44}$$

It is found the pressure required for isentropic implosion of spherical shell is

$$P_{\mathrm{M}} \propto \frac{1}{(t-t_0)^2} \tag{4.45}$$

for $t \longrightarrow t_0$.

4.4 Rayleigh-Taylor instability in pellet implosion

4.4.1 General dispersion relation

Considering two-dimensional x, z perturbation with gravity in the negative z direction $\boldsymbol{g} = -a\boldsymbol{e}_z$, the equation of continuity, momentum conservation equation and condition of incompressibility are given as

$$\frac{\partial \rho}{\partial t} + \nabla \cdot (\rho \boldsymbol{u}) = 0 \tag{4.46}$$

$$\rho \frac{\partial u_x}{\partial t} + \rho \left(u_x \frac{\partial u_x}{\partial x} + u_z \frac{\partial u_x}{\partial z} \right) = -\frac{\partial p}{\partial x} \tag{4.47}$$

$$\rho \frac{\partial u_z}{\partial t} + \rho \left(u_x \frac{\partial u_z}{\partial x} + u_z \frac{\partial u_z}{\partial z} \right) = -\frac{\partial p}{\partial z} - \rho a \tag{4.48}$$

$$\frac{\partial u_x}{\partial x} + \frac{\partial u_z}{\partial z} = 0 \tag{4.49}$$

Here considering a small perturbations around an equilibrium state

$$u_x = u_{x0} + \tilde{u}_x \tag{4.50}$$

$$u_z = u_{z0} + \tilde{u}_z \tag{4.51}$$

$$\rho = \rho_0 + \tilde{\rho} \tag{4.52}$$

$$p = p_0 + \tilde{p} \tag{4.53}$$

which is characterized by

$$u_{x0} = 0 \tag{4.54}$$

$$u_{z0} = 0 \tag{4.55}$$

$$p = p_0 + \tilde{p} \tag{4.56}$$

$$\rho(z, t = 0) = \rho_0(z) \tag{4.57}$$

Then Eqs. (4.46)–(4.49) become

$$\frac{\partial \tilde{\rho}}{\partial t} + \tilde{u}_z \frac{\mathrm{d}\rho_0}{\mathrm{d}z} = 0 \,, \tag{4.58}$$

$$\rho_0 \frac{\partial \tilde{u}_x}{\partial t} = -\frac{\partial \tilde{p}}{\partial x} \,, \tag{4.59}$$

$$\rho_0 \frac{\partial \tilde{u}_z}{\partial t} = -\frac{\partial \tilde{p}}{\partial z} - a\tilde{\rho} \,, \tag{4.60}$$

$$\frac{\partial \tilde{u}_x}{\partial x} + \frac{\partial \tilde{u}_z}{\partial z} = 0 \,. \tag{4.61}$$

Fourier transform of these equations in x and t yields

$$\sigma\tilde{\rho} = -\tilde{u}_z \frac{\mathrm{d}\rho_0}{\mathrm{d}z} \tag{4.62}$$

$$\sigma\rho_0 \tilde{u}_x = -ik\tilde{p} \tag{4.63}$$

$$\sigma\rho_0 \tilde{u}_z = -\frac{\mathrm{d}\tilde{p}}{\mathrm{d}z} - a\tilde{\rho} \tag{4.64}$$

$$ik\tilde{u}_x + \frac{\mathrm{d}\tilde{u}_z}{\mathrm{d}z} = 0 \,. \tag{4.65}$$

Multiplying Eq. (4.63) by ik and using the relation of Eq. (4.65), we obtain

$$k^2\tilde{p} = -\sigma\rho_0 \frac{\mathrm{d}\tilde{u}_z}{\mathrm{d}z} \tag{4.66}$$

And by substituting $\tilde{\rho}$ of Eq. (4.62) into Eq. (4.64), we can find the relation:

$$\frac{\mathrm{d}\tilde{p}}{\mathrm{d}z} = -\sigma\rho_0\tilde{u}_z + \frac{a}{\sigma}\tilde{u}_z \frac{\mathrm{d}\rho_0}{\mathrm{d}z} \,. \tag{4.67}$$

Finally, by eliminating $\tilde{p}$ in these two equations, we can obtain the relation

$$\frac{\mathrm{d}}{\mathrm{d}z}\left(\rho_0 \frac{\mathrm{d}\tilde{u}_z}{\mathrm{d}z}\right) - \rho_0 k^2 \tilde{u}_z = -\frac{k^2}{\sigma^2} a \frac{\mathrm{d}\rho_0}{\mathrm{d}z}\tilde{u}_z \tag{4.68}$$

By multiplying $\tilde{u}_z$ to this we obtain an interesting result:

$$-\frac{\mathrm{d}}{\mathrm{d}z}\left(\rho_0\tilde{u}_z \frac{\mathrm{d}\tilde{u}_z}{\mathrm{d}z}\right) + \rho_0 \left(\frac{\mathrm{d}\tilde{u}_z}{\mathrm{d}z}\right)^2 + \rho_0 k^2 \tilde{u}_z^2 = a\frac{k^2}{\sigma^2}\frac{\mathrm{d}\rho_0}{\mathrm{d}z}\tilde{u}_z^2 \,. \tag{4.69}$$

Then general dispersion relation can be obtained by integrating Eq. (4.69) from $-\infty$ to ∞ with respect to z:

$$\sigma^2 = k^2 \frac{\displaystyle\int_{-\infty}^{\infty} a\frac{\mathrm{d}\rho_0}{\mathrm{d}z}\tilde{u}_z^2 \,\mathrm{d}z}{\displaystyle\int_{-\infty}^{\infty} \rho_0(z)\left[\left(\frac{\mathrm{d}\tilde{u}_z}{\mathrm{d}z}\right)^2 + k^2\tilde{u}_z^2\right]\mathrm{d}z} \,. \tag{4.70}$$

Here boundary condition

$$\lim_{z\to\pm\infty} \tilde{u}_z = 0 \tag{4.71}$$

is considered since perturbations must vanish at infinity.

4.4.2 Classical RTI growth rate

Considering the state in which two fluids with different density is faced at the boundary $z = 0$:

$$\rho_0(z) = \begin{cases} \rho_1 & (z \le 0), \\ \rho_2 & (z \ge 0). \end{cases} \tag{4.72}$$

The condition of continuity of the velocity component normal to the unperturbed boundary is

$$\lim_{z\to 0+} \tilde{u}_z = \lim_{z\to 0-} \tilde{u}_z = \tilde{u}_{z0} \ . \tag{4.73}$$

Assuming uniform density in each region, $\dfrac{\mathrm{d}\rho_0}{\mathrm{d}z} = 0$ for $z \neq 0$; Eq. (4.68) then becomes

$$\frac{\mathrm{d}^2\tilde{u}_z}{\mathrm{d}z^2} - k^2\tilde{u}_z = 0 \tag{4.74}$$

The solution satisfies the boundary condition at infinity (4.71) and the continuity conditions at the interface (4.73) is

$$\tilde{u}_z = \begin{cases} \tilde{u}_{z0}e^{-kz} & (z \ge 0), \\ \tilde{u}_{z0}e^{kz} & (z \le 0). \end{cases} \tag{4.75}$$

Here considering

$$\frac{\mathrm{d}\rho_0}{\mathrm{d}z} = \delta(z)(\rho_2 - \rho_1) \ , \tag{4.76}$$

then the numerator of the dispersion relation (4.70) becomes

$$\int_{-\infty}^{\infty} a\frac{\mathrm{d}\rho_0}{\mathrm{d}z}\tilde{u}_z^2 \,\mathrm{d}z = a(\rho_2 - \rho_1)\tilde{u}_{z0}^2 \ . \tag{4.77}$$

While the denominator of Eq. (4.70) becomes

$$\begin{aligned} \int_{-\infty}^{\infty} \rho_0(z)\left[\left(\frac{\mathrm{d}\tilde{u}_z}{\mathrm{d}z}\right)^2 + k^2\tilde{u}_z^2\right]\mathrm{d}z &= \int_{-\infty}^{\infty} 2\rho_0(z)k^2\tilde{u}_z^2 \,\mathrm{d}z \\ &= \int_{-\infty}^{0} 2\rho_1 k^2\tilde{u}_{z0}^2 e^{2kz}\,\mathrm{d}z + \int_{0}^{\infty} 2\rho_1 k^2\tilde{u}_{z0}^2 e^{-2kz}\,\mathrm{d}z \\ &= \rho_1 k\tilde{u}_{z0}^2\left[e^{2kz}\right]_{-\infty}^{0} - \rho_2 k\tilde{u}_{z0}^2\left[e^{-2kz}\right]_{0}^{\infty} \\ &= (\rho_1 + \rho_2)k\tilde{u}_{z0}^2 \ . \end{aligned} \tag{4.78}$$

Substituting them into Eq. (4.70), yielding

$$\sigma^2 = \frac{\rho_2 - \rho_1}{\rho_1 + \rho_2}ak \equiv A_t ak \ . \tag{4.79}$$

This is the classical growth rate of R-T instability σ_{RT}.

4.4.3 Density gradient

Now considering a region with variable density $\rho(z)$ joins two homogeneous regions with different densities ρ_1 and ρ_2. For simplicity, we consider the case of the following model density profile;

$$\rho_0(z) = \begin{cases} \rho_1 + \dfrac{\Delta\rho}{2} e^{2z/L} & (z \le 0), \\ \rho_2 - \dfrac{\Delta\rho}{2} e^{-2z/L} & (z \ge 0). \end{cases} \tag{4.80}$$

where $\Delta\rho = \rho_2 - \rho_1$. In this case the numerator and denominator of Eq. (4.70) become

$$\int_{-\infty}^{\infty} a \frac{\mathrm{d}\rho_0}{\mathrm{d}z} \tilde{u}_z^2 \, \mathrm{d}z = k\tilde{u}_{z0}^2(\rho_1 + \rho_2) \tag{4.81}$$

and

$$\int_{-\infty}^{\infty} \rho_0(z) \left[\left(\frac{\mathrm{d}\tilde{u}_z}{\mathrm{d}z} \right)^2 + k^2 \tilde{u}_z^2 \right] \mathrm{d}z = \frac{a\Delta\rho\tilde{u}_{z0}^2}{1+kL} \,, \tag{4.82}$$

respectively. Then substituting eqns. (4.81) and (4.4.3) into Eq. (4.70), we obtain

$$\sigma = \sqrt{\frac{ak}{1+kL} \frac{\rho_2 - \rho_1}{\rho_1 + \rho_2}} = \sqrt{\frac{A_t ak}{1+kL}} \,. \tag{4.83}$$

Here taking the limit of perturbation wavelength, we find

$$\sigma \to \begin{cases} \sigma_{\mathrm{RT}} & \text{if } kL \ll 1, \\ \sqrt{\dfrac{A_t a}{L}} & \text{if } kL \ll 1. \end{cases} \tag{4.84}$$

Here the density scale length

$$\frac{\rho_0}{\mathrm{d}\rho_0/\mathrm{d}z} = \frac{\rho_0}{\Delta\rho L e^{-2|z|/L}} \tag{4.85}$$

has the its minimum value

$$L_{\min} = \frac{(\rho_1 + \rho_2)/2}{(\rho_2 - \rho_1)L} = \frac{L}{2A_t} \tag{4.86}$$

at $z = 0$, then for $kL \ll 1$, the growth rate becomes

$$\sigma \to \sqrt{\frac{a}{2L_{\min}}} \,. \tag{4.87}$$

For practical application, it is known that

$$\sigma = \sqrt{\frac{A_t ak}{1 + A_t kL_{\min}}} \tag{4.88}$$

gives a good approximation of the growth rate.

4.4.4 Stabilization effect by ablation velocity

In the case of the classical R-T instability, perturbation ζ grows by the formula;

$$\zeta(z,t) = \zeta_0(z) e^{\sigma_{\mathrm{RT}} t} e^{-k|z|} \,, \tag{4.89}$$

where ζ_0 is the initial perturbation amplitude. Let u_a is the ablation velocity, the perturbation growth by a factor $e^{\sigma_{RT}\Delta t}$ but interface simultaneously penetrates to depth $\Delta z = u_a \Delta t$ inside a dense materials in the time interval Δt. This effect reduce the growth rate by a factor $e^{-ku_a\Delta t}$ and the effective growth rate is expected to be

$$\sigma = \sqrt{ak} - ku_a \,. \tag{4.90}$$

In practice, the following famous formulae, Takabe's formula and modified Takabe's formula,

$$\sigma = \alpha_1\sqrt{ak} - \beta_1 ku_a \qquad (\mathcal{F} \gtrsim 1.0), \tag{4.91}$$

$$\sigma = \alpha_2\sqrt{\frac{ak}{1+kL_{\min}}} - \beta_2 ku_a \qquad (\mathcal{F} \lesssim 0.1), \tag{4.92}$$

are known to give fairly good approximation [36]. Here $\mathcal{F}$ is the Froude number

$$\mathcal{F} \equiv \frac{u_a^2}{aL_0}, \tag{4.93}$$

which is the dimensionless value defined as the ratio of inertial force of the fluid and the gravity force (in this case the inertial force by the ablative acceleration) works on it (L_0 is the characteristic length of the system). ν is the exponent used to describe the temperature dependence of thermal conductivity of the fluid:

$$\chi = \chi_0 T^\nu \,. \tag{4.94}$$

As shown in Fig. 4.3, α_1, α_2, β_1, β_2 are the function of ν and $\mathcal{F}$ and for wide parameter range, $0.9 < \alpha_1 < 1.0$, $0.9 < \alpha_2 < 1.1$, and β_1, $\beta_2 \geq 1.2$ (in case of $\mathcal{F} \ll 1$ and $\mathcal{F} \gg 1$ they fast grows to a large value).

By the stabilizing effect due to ablation velocity, the growth of short wavelength mode ($l \gg 1$), which has large growth rate in classical R-T instability, is suppressed and the mode with perturbation wavelength smaller than a certain threshold value is perfectly stabilized.

4.4.5 Perturbation growth in the acceleration phase

According to the linear theory, the amplitude of mode l perturbation at the ablation surface is give by

$$\zeta_l^{\text{out}} = \zeta_{l0}^{\text{out}} G_l^{\text{out}} \tag{4.95}$$

where ζ_{l0}^{out} is the initial perturbation amplitude,

$$G_l^{\text{out}} = \exp\left(\int_0^t \sigma_l(t')\,\mathrm{d}t'\right) \tag{4.96}$$

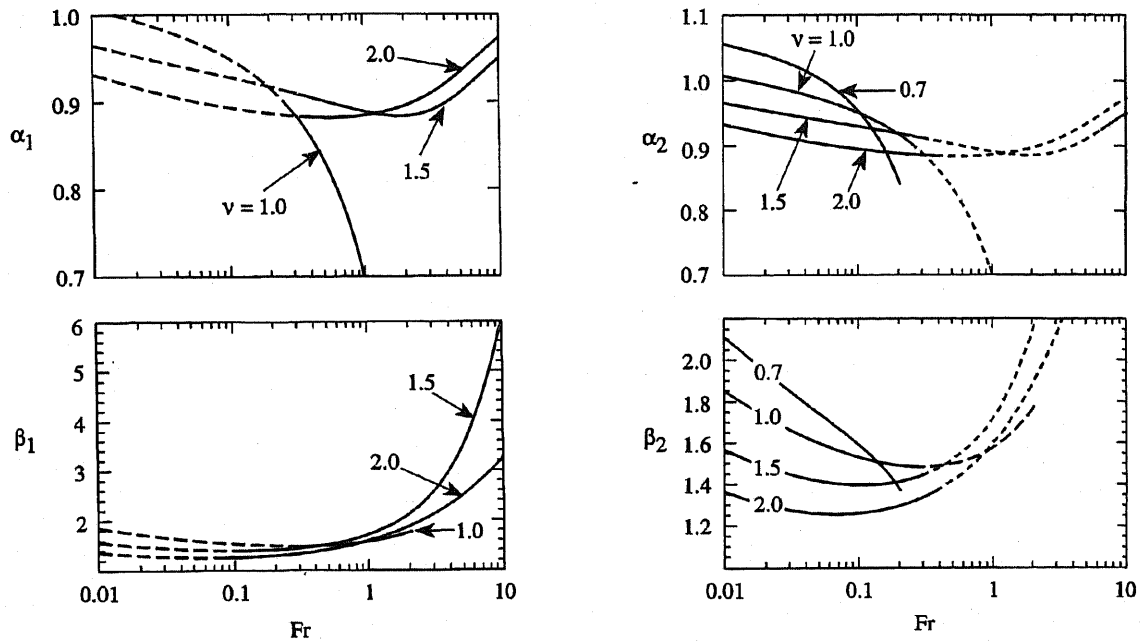

Fig. 4.3: Dependence of the parameters α_1, α_2, β_1, β_2 of Takabe's formula (Eq. (4.91)) and modified Takabe's formula (Eq. (4.92)) on Froude number $\mathcal{F}$ and the coefficient ν (FIG. 5 and 6 from reference [36])

is the growth factor, and σ_l is the linear growth rate of mode l perturbation. The linear growth rate is given in Eq. (4.92) by replacing $k = l/R$ for considering spherical geometry;

$$\sigma_l = \alpha_2 \sqrt{\frac{al/R}{1 + lL_{\min}/R}} - \beta_2 \frac{l}{R} u_a \,. \tag{4.97}$$

To avoid collapse of the pellet during the implosion, the condition

$$\zeta(t) \ll \Delta R(t) \tag{4.98}$$

must be satisfied at any time during the implosion. Then in the hydrodynamic simulation, the value of a, $L_{\min}$ and u_a is traced over the whole calculation period and the growth rate is estimated. Since it is considered that initial perturbations have a wide spectrum and random phases, the amplitude in Eq. (4.98) is given by

$$\zeta \approx \sqrt{2}\zeta_{\rm rms} = \sqrt{2 \sum_l \frac{\zeta_l^2}{2l+1}} \,. \tag{4.99}$$

However, in the simulation, the growth factor of the fastest growing mode is recorded. Since the growth factor of the fastest growing mode is much larger than that of the other modes, this approximation produces little error in the estimation.

4.5 Calculation results

4.5.1 Optimum core plasma design for the fast ignition scheme

Before entering the description of the details of the calculation model and results, we mention the purpose and direction of this simulation study.

The fast ignition method not only reduce the energy for implosion but also provides several merits in the implosion. One of these merit worth to be mentioned is the possibility of implosion with small velocity. The idea of this low velocity implosion is originated from a simple scaling for the central ignition. The energy required to generate hot spot with radius $\xi_s R$ (R is the entire radius of compressed fuel) in isobaric state is scaled with the parameters of hot spot as the following manner.

The density of fuel ρ_c surrounding the hot spot can be written with the total mass of the fuel M and the parameter ξ_s given in the above as

$$\rho_c = \frac{\frac{3M}{4\pi R^3} - \rho_s \xi_s^3}{1 - \xi_s^3} \,. \tag{4.100}$$

Then using energy conservation law

$$E = \frac{1}{2} M v_{imp}^2 = \frac{3}{2} P \frac{4}{3} \pi R^3 \tag{4.101}$$

and equilibrium pressure

$$P = K \rho_s T_s, \tag{4.102}$$

Eq. (2.84) can be transformed into the form:

$$\begin{aligned} \rho_c &= \frac{\frac{3P}{v_{imp}^2} - \rho_s \xi_s^3}{1 - \xi_s^3} \\ &= \frac{3P}{v_{imp}^2} \frac{1 - \frac{\xi_s^2 v_{imp}^2}{3KT_s}}{1 - \xi_s^3} \\ &= \frac{3P \Lambda_E^{\frac{1}{5}}}{v_{imp}^2 (1 - \xi_s^3)} \,, \end{aligned} \tag{4.103}$$

where

$$\Lambda_E^5 \equiv 1 - \frac{\xi_s^2 v_{imp}^2}{3KT_s} \,. \tag{4.104}$$

The energy required to achieve implosion is obtained by using Eq. (4.101) as

$$
\begin{aligned}
E &= \frac{3}{2}\frac{4}{3}\pi R^3 \\
&= 2\pi R^3 P \\
&= 2\pi R^3 \left(P_* \alpha \rho_c^{\frac{5}{3}}\right) \\
&= 2\pi R^3 \frac{\left(P_* \alpha \rho_c^{\frac{5}{3}}\right)^3}{P^2} \\
&= \frac{2\pi R^3 P_*^3 \alpha^3}{P^2} \frac{3^5 P^5 \Lambda_E}{v_{\mathrm{imp}}^{10}\left(1-\xi_{\mathrm{s}}^3\right)^5} \\
&= 2\pi R^3 P_*^3 \alpha^3 \times 3^5 \left(K \rho_{\mathrm{s}} T_{\mathrm{s}}\right)^3 \frac{\Lambda_E}{v_{\mathrm{imp}}^{10}\left(1-\xi_{\mathrm{s}}^3\right)^5} \\
&= 3^5 \times 2\pi \left(K P_*\right)^3 \frac{\alpha^3 \left(\xi_{\mathrm{s}} \rho_{\mathrm{s}} R\right)^3 T_{\mathrm{s}}^3 \Lambda_E}{v_{\mathrm{imp}}^{10} \xi_{\mathrm{s}}^3 \left(1-\xi_{\mathrm{s}}^3\right)^5} \\
&= 3^5 \times 2\pi \left(K P_*\right)^3 \frac{\alpha^3 \left(H_{\mathrm{s}} T_{\mathrm{s}}\right)^3}{v_{\mathrm{imp}}^{10} \xi_{\mathrm{s}}^3 \left(1-\xi_{\mathrm{s}}^3\right)^5} \Lambda_E \ ,
\end{aligned}
\tag{4.105}
$$

where $H_{\mathrm{s}} \equiv \rho_{\mathrm{s}} R_{\mathrm{s}} = \rho_{\mathrm{s}} \xi_{\mathrm{s}} R$. Then the simple scaling

$$
E \propto \frac{\alpha^3 H_{\mathrm{s}}^3 T_{\mathrm{s}}^3}{v_{\mathrm{imp}}^{10}} \tag{4.106}
$$

is obtained if $\Lambda_E \sim 1$.

One immediately can see a large value of implosion velocity v_{imp} is demanded to generate the hot spot which has high areal density and high temperature with low driver energy. Thus relatively thin (high aspect ratio of ~ 10) pellet tends to be used in the central ignition method because thin pellet can attain high implosion velocity in isentropic compression, as discussed in section 4.3 (see Eq. (4.42)). But the pellet with high initial aspect ratio also has high in-flight aspect ratio (IFAR), the aspect ratio at each time of implosion, and the collapse of the pellet due to the growth of Rayleigh-Taylor instability is concerned. By contrast, in case of the fast ignition, it is not needed to generate high temperature in the center of compressed fuel. Thus it is expected to achieve high gain with small implosion velocity, which may enable the use of the pellet with low initial aspect ratio. However, in fast ignition scheme high density of the pellet also required to suppress the energy required for the fast heating, as described in the section 2.1.6. Then the key point in the core plasma design for the fast ignition scheme is to achieve high density compression with utilizing the characteristics of capability of low velocity implosion.

Though Eq. (4.106) is quite preliminary one obtained from a simple model, its dependence on the parameters is in fairly good agreement with the results of numerical simulation [37–39]. Several scalings have been proposed as the revision of Eq. (4.106) through the numerous theoretical and numerical works by many researches, and optimization of the pellet design and laser pulse shaping has been explored.

Among them, the adiabat shaping method by using an ultra short and high intensity pre-pulse ($\sim$ 0.1 ns, $\sim$ 100 TW) proposed by Betti *et al.* [40] is remarkable because they achieve high density ($\sim$ 300 g/cm^3) compression by using a pellet with very low initial aspect ratio ($A_0 \simeq 2$).

Since there are high degree of freedom in the design of the pellet and laser pulse shape, it may be possible to find the optimum design of core plasma for this reactor design study. However, the main purpose of this simulation is to demonstrate the design point estimated by the 0-D analysis. Then we used as a simple model as possible to grasp the design direction definitely.

4.5.2 Pellet design and laser pulse shaping

Most of researches in laser fusion adopt a cryogenic D-T fuel pellet, spherical hollow shell of D-T ice layer surrounded by the thin plastic (hydrocarbon) ablator. In this design study, we also adopted the same type fuel pellet. Figure 4.4 describes the schematic viewing of the pellet using the calculation. For the plastic ablator, hydrocarbon which consists of the same amount of carbon and hydrogen is used. In the parameter scan, the total mass of the D-T fuel was fixed to be the same value estimated by the 0-D calculation in chapter 3, $M_f = 0.57$ mg, and the aspect ratio $A_0 = \Delta R_0/R_0$ and the thickness of ablator ΔR_a were scanned.

For the laser pulse shaping, simple formula obtained by the theory (Eq. (4.45)) is used. However, the power given by Eq. (4.45) diverges at the collapse time $t = t_c$. Then we divide the laser pulse into two parts: the region in which the power grows after Eq. (4.45) (main pulse) and the region in which the power keeps a constant value (flat-top). Then we selected the time evolution of the laser power P as the following:

$$P(t) = \begin{cases} \dfrac{a}{\sqrt{t - \tau_m - (P_{ft}/a)^2}} & t \le \tau_m, \\ P_{ft} & \tau_m \le t \le \tau_m + \tau_{ft}. \end{cases} \tag{4.107}$$

Here τ_m, τ_{ft} are the duration of main pulse and flat-top, respectively, and a is a proportional factor. An example of laser pulse shape is shown in Fig. 4.5. Then laser pulse shape is uniquely defined when four of the following five parameters are given;

- main pulse duration τ_m
- flat-top duration τ_{ft}
- the power of flat-top P_{ft}
- proportional factor a
- total energy E

In this calculation, τ_m, P_{ft}, a were given and τ_{ft} was adjusted so that the total energy was equal to 350 kJ.

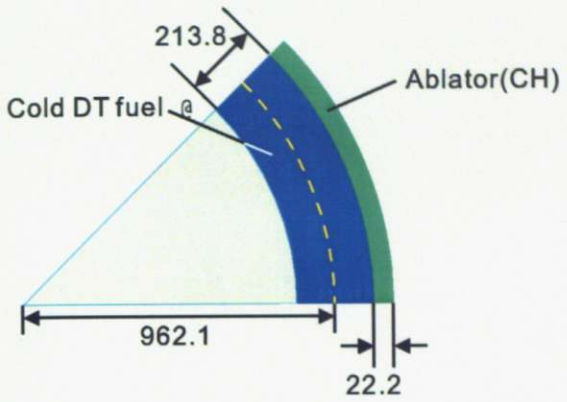

Fig. 4.4: Schematic viewing of the fuel pellet in case of $A_0 = 4$.

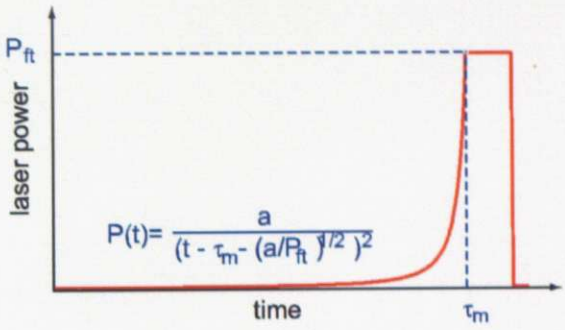

Fig. 4.5: An example of laser pulse shape used in the simulation

4.5.3 Demonstration of the target design point

To demonstrate the target design point estimated in 0-D analysis ($G = 100$ with $E_c = 350$ kJ and $E_h = 50$ kJ), the following three factors need to be considered:

- achievement of high ρR value which enables sufficient burn fraction to obtain high gain,
- achievement of high density to suppress the heating energy,
- suppression of the growth of Rayleigh Taylor instability to avoid the collapse of the pellet during implosion.

Then we performed calculations with the pellet with several initial aspect ratio to clarify the dependence of density, ρR value and growth rate of R-T instability on the pellet design and laser pulse shaping. Figure 4.6–4.9 show the dependence of the achieved maximum areal density and the peak density value at the timing of the maximum areal density is achieved on the parameters given for the laser pulse shaping; proportional factor a and the power of the flat-top region P_{ft}. In these calculations, main pulse duration was fixed to be 26 ns. One can see there is the optimum point for each parameter. It also can be seen the tendency that optimum point shifts in high peak power side and low proportional factor side as the initial aspect ratio increases.

Table 4.1 lists the parameters from the data for each initial aspect ratio which achieve the maximum areal density within this parameter scan. Figure 4.10 show the density profiles at the maximum compression for each data. It is clearly seen that the achieved maximum ρR value is almost independent of

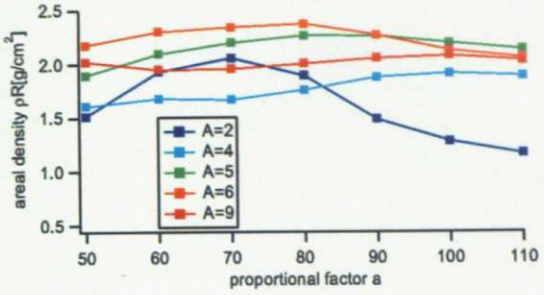

Fig. 4.6: The dependence of the maximum areal density ρR on the proportional coefficient a for various initial aspect ratio.

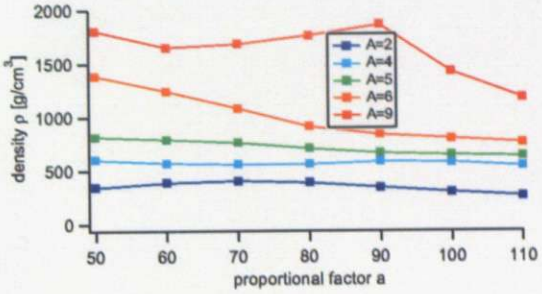

Fig. 4.7: The dependence of the peak value of the density ρ on the proportional coefficient a for various initial aspect ratio when the maximum areal density is achieved.

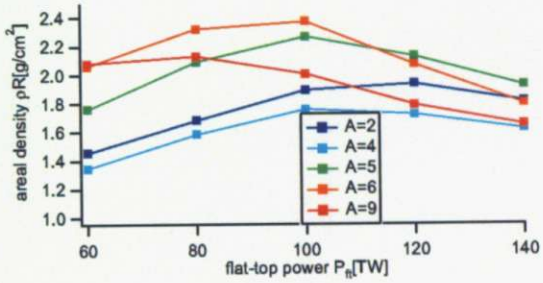

Fig. 4.8: The dependence of the maximum areal density ρR on the laser power of flat-top region P_{ft} for various initial aspect ratio.

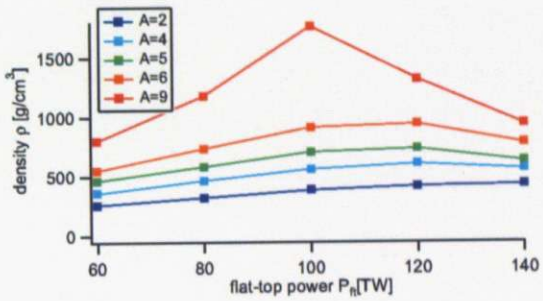

Fig. 4.9: The dependence of the peak value of the density ρ on the laser power of flat-top region P_{ft} for various initial aspect ratio when the maximum areal density is achieved.

the initial aspect ratio. One can also see the pellet with lower initial aspect ratio is compressed with smaller implosion velocity and smaller IFAR, as expected in the theory. However, the density peak value at the time when the maximum ρR value is achieved is much higher for the pellet with a large initial aspect ratio. In addition, shell thickness ΔR at the time when IFAR peaks does not depend so much on the initial aspect ratio because the data that has high IFAR tends to have small shell inner radius and both effects are canceled out. The growth rate of R-T instability of the fastest growing mode $G_{l,\max}$ is also independent of the initial aspect ratio. Then the acceptable maximum amplitude of initial perturbation ζ_{l0} on the pellet surface $\Delta R/G_{l,\max}$ also does not depend so much on the initial aspect ratio. Consequently, there is no superiority in the pellet with low initial aspect ratio for the suppression of growth of R-T instability within the scope of this analysis. Then the pellet with higher initial aspect ratio is favorable for high density compression. However, the pellet with high initial aspect ratio has a strongly peaked density profile at the timing of the maximum compression. Then the R-T instability in stagnation phase that causes the mixing of the hot spot region and the dense cold fuel region, may be

concern. This fact may give an upper limit for the initial aspect ratio.

Table 4.1: Comparison of parameters related to the implosion for various initial aspect ratio

R [μm]	A	ΔR_a [μm]	τ_m [ns]	a	P_{ft} [TW]	$(\rho R)_{max}$ [g/cm^2]	ρ_{max} at $(\rho R)_{max}$ [g/cm^3]	v_{imp} [10^5m/s]	A_{inf}^{peak}	$G_{l,max}$	ΔR at A_{inf}^{peak} [nm]	allowable ζ_{l0} [nm]
630.8	2	38.7	26.2	70	115	2.174	486.1	2.75	57.5	97.3	100.2	1.03
855.2	4	22.2	26.4	96	120	2.128	703.3	2.42	62.0	55.0	87.3	1.59
935.5	5	26.0	26	86	95	2.271	699.1	2.45	92.1	66.5	75.6	1.14
1004.6	6	25.5	25.6	86	90	2.222	813.7	2.75	105.6	54.1	70.9	1.31
1170.5	9	22.1	26.2	90	90	2.123	1565.4	3.10	155.4	52.4	55.4	1.06

Next we examine the achievable fusion gain of each case. By adding an external heating, in all cases the pellet reaches ignition. However, in case of the pellet with a low initial aspect ratio, the achieved fusion gain is smaller than that estimated by the 0-D analysis model. For example, the achieved gain for the pellet with $A_0 = 4$ is 75 when the heating energy is 10 kJ. The fusion gain slightly increases with the increase of the heating energy, but it saturates at 81 with the injection energy of 15 kJ. If the heating energy increases more, fusion gain slightly decreases because fusion energy output does not change regardless the amount of the heating energy. By contrast, fusion gain $G = 100$ is achieved by the pellet with $A_0 \geq 6$. In this case, $G \sim 100$ is already achieved with 10 kJ heating energy, which is the same value estimated by the 0-D model.

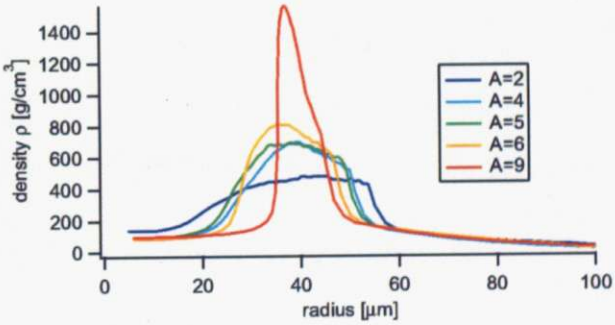

Fig. 4.10: Comparison of density profiles for different initial aspect ratio.

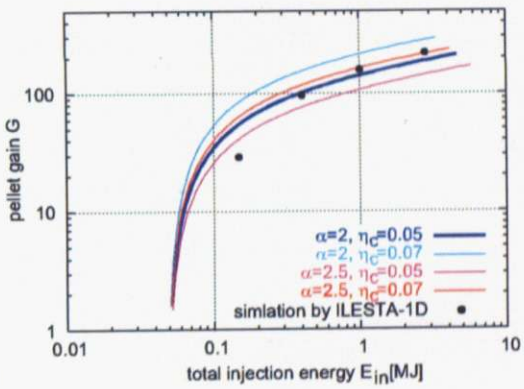

Fig. 4.11: Comparison of fusion gain dependence on injection energy obtained from the 1-D hydrodynamic simulation results (black circles) with gain curves estimated by using the 0-D model (color lines).

Then we compared the results of the 1-D hydrodynamic simulation with the 0-D analysis model by using the 1-D simulation data for the pellet with $A_0 = 6$. Figure 4.11 shows the comparison of one dimensional hydrodynamic simulation (black circle) with the zero-dimensional analytic model (broken line). The data selected for the 1-D simulation result are the ones that achieve the highest areal density

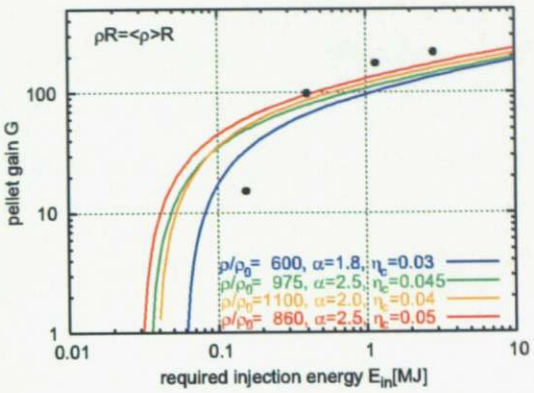

Fig. 4.12: Comparison of gain dependence on injection energy obtained from the 1-D hydrodynamic simulation results (black circles) with gain curves estimated by using the 0-D model (color lines). Each curve is calculated by using implosion parameters obtained from the corresponding 1-D simulation result.

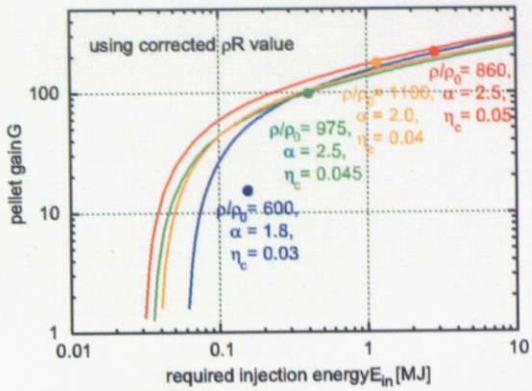

Fig. 4.13: Comparison of gain dependence on injection energy obtained from the 1-D hydrodynamic simulation results (black circles) with gain curves estimated by using the 0-D model (color lines). Each curve is calculated by using implosion parameters value obtained from the corresponding 1-D simulation result with correction of ρR value according to the 1-D simulation result.

with the injection energy around the plotted point. Seemingly, both results are in good agreements. However, actually both coupling efficiency of the implosion laser and the averaged isentrope are different from 0-D estimation. Coupling efficiency tend to be smaller than 0-D estimation ($\eta_c = 0.3$–0.5) and isentrope factors tend to be larger ($\alpha = 2$–3) than 0-D estimation. Both give a negative effect that increases the required energy for implosion. Then the average densities in 1-D simulations are all smaller than 0-D estimation value (300 g/cm^3). Figure 4.12 shows the gain curves calculated by 0-D model with the same implosion parameter sets estimated from the 1-D simulation results. One easily can see the estimated gain by 0-D model is smaller than that obtained from 1-D simulation. Whereas all the 1-D simulation results have peaked density profile and ρR value of them is 1.2–1.5 times larger than that calculated from the average density. Figure 4.13 shows the gain curves calculated by the same manner as Fig. 4.12 but using corrected ρR values according to the 1-D simulation. One can see each curves are in good agreement with the corresponding 1-D result except for the one with the lowest injection energy. This fact means 0-D analysis model can provide accurate prediction of fusion gain if the new parameter, the correction coefficient of ρR value due to the effect of the peaked density profile, is included in the calculation.

However, 0-D model predicts that the achievable fusion gain, i.e, burn fraction only depends on the areal density. If this prediction is true, the pellet with lower initial aspect ratio can also achieve fusion gain of 100. It was found that the difference in fusion gain in 1-D simulations was caused by the difference in radial density profile around the heating region. Since the energy deposition of additional

electron heating is proportional to the density of each mesh, most of energy is deposited around the inner edge region of the density peak and temperature in the region increases. This high density and high temperature at the inner edge region generates extremely high pressure and re-compresses the rarefied gas in the pellet center, resulting in the increase of the temperature of the gas. It also pushes the density peak to outwards, resulting in the formation of the further peaked density profile. The high temperature center region becomes a source of alpha particles and the high density region stops the alpha particle and absorbs the energy and then ignites and burns. The pellet with low A_0 has a smaller peak density value and then this effect becomes weak. This is the reason why the fusion gain differs by the initial aspect ratio. However, such effect cannot be expected in actual asymmetric heating because of the relatively flat density profile of heating region. The pressure work is also not expected due to the loss from the backward free surface.

Then we also performed two-dimensional calculation of heating and burning through the collaboration with Dr. T. Johzaki in the Institute of Laser Engineering (ILE), Osaka University in order to clarify the properties of the fast heating.

2-D calculation was carried out in the hemicycle region by assuming axial symmetry (see Fig. 4.14). Radial profiles of all physics parameters (e.g., density, temperature, ionization, etc.) were initially given according to the 1-D simulation results at the timing of maximum compression. Then the shape of heating region became a cylinder on the edge of spherical pellet. Here the radius of heating region was set to be 15 μm and the depth of heating region was adjusted to maximize fusion gain (typical value is $\rho L = 1.8$ g/cm^2). Figure 4.15 shows the dependence of fusion gain on the heating energy for 5 cases of density and temperature profile at the maximum compression. Here all data are obtained by 1-D simulation of the pellet with $A_0 = 4$ and implosion laser energy of 350 kJ. The corresponding density and temperature profiles and the laser pulse shape are shown in Figs. 4.16 and 4.17. Then one can find the existence of a threshold heating energy to achieve ignition and burn of the fuel. One can also see this threshold energy only depends on the peak density of the compressed core and does not depend on the density and temperature profiles. In the case that the peak density is about 800 g/cm^3, fusion gain of $\sim$ 100 is achieved with 10 kJ heating energy. Rather much higher gain ($\sim$ 120) is achieved with slightly higher heating energy. Thus the design point predicted in 0-D analysis can be obtained if the pellet is compressed to has sufficient areal density (> 2 g/cm^2) and the high peak density ($\sim$ 800 g/cm^2). Figure 4.17 indicates higher peak density is achieved by the higher peak power of the implosion laser. If the total energy of implosion laser is limited, the pulse shape with a low pre-pulse power and a long main pulse duration is favorable to achieve high flat-top power at the final phase. But such a high

peak power at the final phase of implosion causes high laser intensity, which leads to several laser-plasma instabilities on the pellet surface. Especially two plasmon decay generates high energy ($\sim$ keV) electrons that causes preheat of the cold fuel. This instability grows when the intensity substantially exceeds 10^{14} W/cm^2. Thus a careful selection of a laser pulse shape is required to achieve the sufficient peak density for minimizing the heating energy.

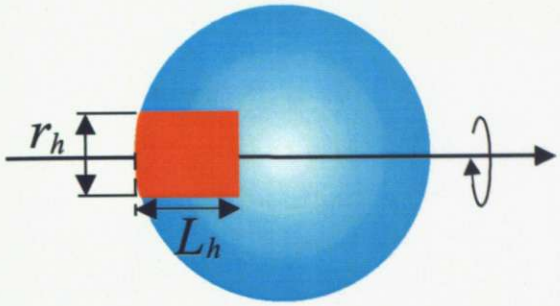

Fig. 4.14: Schematic view of the calculation model used in the 2-D simulation of fast heating.

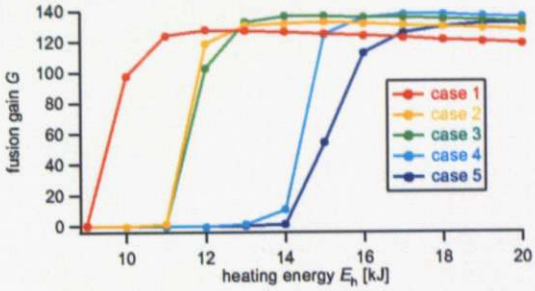

Fig. 4.15: Dependence of fusion gain on the core heating energy for 5 cases of implosion for the pellet with $A_0 = 4$ and 350 kJ implosion laser.

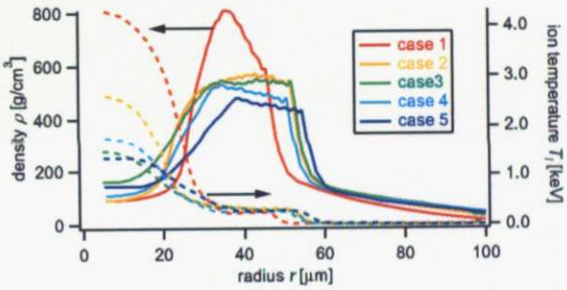

Fig. 4.16: Density and ion temperature profiles for the each implosion cases

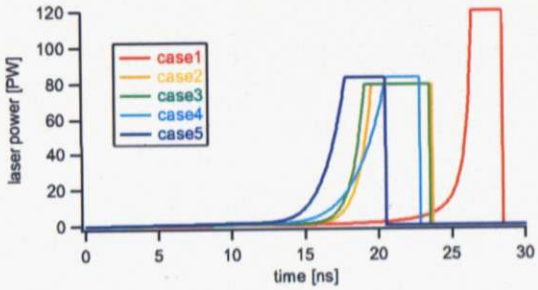

Fig. 4.17: Laser pulse shapes for the each implosion cases

4.6 Summary and proposal

In the core plasma design, the optimum design of pellet and laser pulse shaping for this design concept has been examined. 1-D hydrodynamic simulation reveals :

- The coupling efficiency of implosion laser and isentrope factor are in the range of 0.03-0.05 and 2-2.5, respectively.
- Although the above values lead to lower average density than the estimation by 0-D analysis, the maximum areal density value is almost the same value expected in zero-dimensional model by the enhancement effect on the areal density due to the density peaking.

- The maximum areal density does not depend so much on the initial aspect ratio of the fuel pellet. Whereas the peak density at the maximum compression increases with increasing the initial aspect ratio.
- The growth rate of the Rayleigh-Taylor instability during implosion also does not depend so much on the initial aspect ratio.

We also carried out two dimensional hydrodynamic simulation to clarify the characteristics of the fast heating. Then it was found that:

- there is a threshold heating energy for ignition and burn of the compressed fuel.
- this threshold energy only depends on the peak density of the compressed fuel and the energy decreases with increasing of the peak density

These results indicates that the pellet with high initial aspect ratio is favorable because it can be compressed to high density, resulting to the reduction of required heating energy, within the simple laser pulse shape based on the theory of isentropic compression of hollow shell. However, highly peaked density profile can cause the mixture of the high density cold fuel and low density hot center region due to the growth of R-T instability at stagnation phase. This may give an upper limit in the initial aspect ratio.

In the case that the pellet with initial aspect ratio of 4 was imploded by a laser with the peak power of 120 TW and the total energy of 350 kJ, the peak density reached to 800 g/cm^3. In this case, pellet gain $G = 100$ was achieved with the net core heating energy of 10 kJ. This result indicated if the coupling efficiency of heating laser to the compressed core can be 20 %, the sufficient high gain can be achieved with 400 kJ laser (350 kJ for implosion and 50 kJ for heating). This value coincides to that estimated by the simple 0-D physics model. Then design point of FALCON-D was successfully demonstrated.